Towards an alloy design strategy by tuning liquid local ordering: What solidification of an Al-alloy designed for laser powder bed fusion teaches us

Maxence Buttard, Guilhem Martin, Xavier Bataillon, Gilles Renou, Pierre Lhuissier, Julie Villanova, Béchir Chehab, Philippe Jarry, Jean-Jacques Blandin, Patricia Donnadieu

Towards an alloy design strategy by tuning liquid local ordering: what solidification of an Al-alloy designed for laser powder bed fusion teaches us

Maxence BUTTARD[1], Guilhem MARTIN[1*], Xavier BATAILLON[1], Gilles RENOU[1], Pierre LHUISSIER[1], Julie VILANOVA[3], Béchir CHEHAB[2], Philippe JARRY[2], Jean-Jacques BLANDIN[1], Patricia DONNADIEU[1]

1. Univ. Grenoble Alpes, CNRS, Grenoble INP, SIMAP, F-38000 Grenoble

2. Constellium Technology Center, Parc économique Centr'Alp, 725, rue Aristide-Bergès, CS 10027, 38341 Voreppe cedex, France

3. ESRF – The European Synchrotron, 71 avenue des Martyrs 38043 Grenoble, France

*Corresponding author: maxence.buttard@grenoble-inp.fr

Abstract

High-strength aluminium alloys from the 2XXX, 6XXX, and 7XXX series suffer from severe hot cracking issues during 3D printing. Thus, there is a need to design new alloys with an improved hot cracking resistance while taking advantage of the non-equilibrium processing conditions of laser powder bed fusion to achieve optimized properties. Here, we report the successful fabrication of a new Al-Mn-Ni-Cu-Zr alloy designed for L-PBF. The as-built microstructure was characterized at different scales using synchrotron X-ray nano-tomography and microscopy with a special focus on automated crystallographic orientation mapping (ACOM) in transmission electron microscopy. Based on this multiscale microstructural investigation, we identify various mechanisms involving the presence of a locally ordered liquid during solidification under conditions typical of additive manufacturing. This local liquid ordering is often defined as Icosahedral Short Range Order (ISRO). The multiple consequences of ISRO in the liquid on the hierarchical microstructure inherited from additive manufacturing are discussed. ISRO enables refinement of the grain size thus improving the processability via an increase of the hot cracking resistance, producing equiaxed grains and twinned dendrites contributing to randomizing the crystallographic texture, and possibly extending supersaturated solid solutions through a cage effect. It is concluded that promoting ISRO should be considered a promising pathway to design alloys for additive manufacturing with good processability and optimized properties.

Keywords: Solidification; Al-alloys; Icosahedral Short Range Order (ISRO); Microstructure; Additive Manufacturing; TEM

1. Introduction

Laser powder bed fusion is becoming more and more popular in the industry because this new processing route allows the fabrication of metallic components exhibiting sophisticated geometries while possibly reducing post-fabrication operations. Besides the high degree of freedom offered by L-PBF, the high cooling rates inherent to L-PBF generate out-of-equilibrium microstructures allowing unprecedented properties to be achieved [1]–[4]. Aluminium alloys inherited from casting such as the Al-Si near-eutectic grades have been proven to be processable by additive manufacturing but suffer from limited mechanical performances [5]–[7]. High-strength Al-alloys such as the 2XXX, 6XXX, or 7XXX series are often classified as difficult to process using L-PBF due to the development of hot cracks during fabrication [8]–[14]. Their microstructures are anisotropic in terms of morphology with large columnar grains elongated along the building direction, and showing a strong <001> or <110> crystallographic texture. Such textures result from epitaxial growth from the underlying layers or adjacent tracks. <001> textures are often found because this is the typical direction associated with the fastest growth rate in metals showing a cubic lattice structure. <110> textures are also often observed in AM materials because of epitaxial growth between adjacent tracks because of the side-branching mechanism. Side branching is defined as a mechanism allowing the growth of grains along with orthogonal directions in response to changes in the local thermal gradient direction. Grain refinement was proven to be an efficient strategy to overcome hot cracking issues. The idea consists in introducing nucleating agents via the addition of exogenous particles such as TiB_2 [15], [16] or LaB_6 [17], [18], or solutes such as Zr [19]–[23], Sc [3], [24]–[26], Nb [10], [27] or Ti [27]–[29] known to precipitate the primary metastable phase Al_3X-$L1_2$ (X = Zr, Sc, Ti, Nb). Those inoculant particles or primary phases show a very small lattice misfit with the Al-matrix, a key feature to be an efficient grain refiner [30], [31]. Based on the pioneering work of Turnbull and Vernnegut [31] and refined a few years later by Bramfitt [30], the lattice misfit parameter δ should be kept below 12% to be efficient with respect to heterogeneous nucleation. In addition, improving the processability of high-strength alloys contributes to breaking the anisotropy of the 3D printed parts and increasing the yield strength at room temperature via a Hall-Petch effect with a grain size usually achieved using severe plastic deformation (typically < 1 μm).

Since the pioneering work of Frank in 1952 [32] suggesting the presence of Icosahedral Short Range Order (ISRO) in undercooled liquids, the latter is not necessarily perceived as a fully disordered phase. The discovery of quasi-crystals by Schechtman [33] gave substance to the idea of Frank that the liquid can be icosahedrally ordered over short distances. Indeed, QCs with 5-fold symmetry have been observed in many metallic systems, in particular, in binary Al-X alloy where X is a transition metal with (X = Mn, Cr…), see e.g. [28], [29]. ISRO in the liquid was also largely discussed in the literature of bulk metallic glasses because it is suspected to impede crystallization and thus enables retaining an amorphous structure [34], [35]. On the opposite, ISRO-based mechanisms have been shown to influence the nucleation and growth of some Al-alloys as highlighted in Rappaz et al. [36]. For example, adding 1000 ppm of Cr in binary cast Al-Zn alloys lead to a remarkable grain refinement that goes along with an unexpected fraction of Σ3 twin boundaries [37]. Σ3 twin boundaries are not expected in Al alloys because of their high stacking fault energy. Based on in-depth crystallographic studies, clusters of grains where nearest neighbors were found to be related by twinning relationships, have been identified. Such multiple twinning relationships among nearest neighbor grains supported the idea that FCC Al grains nucleate from an icosahedral template via an epitaxial relationship where the <111> directions of the FCC unit cell of Al are parallel to the 3-fold axes of the icosahedron, and the <110>-directions of the FCC unit cell of Al are parallel to the 5-fold axes of the icosahedron. The nucleation mechanism proposed by Kurtuldu et al. in [38] suggests the formation of the FCC-phase on icosahedral quasicrystals (iQCs) during solidification but those quasi-crystalline phases made of icosahedral building blocks have not been observed or were assumed to disappear via a peritectic transformation. Similar mechanisms were also found in cast Au-alloys with minute addition of Ir [38].

ISRO-based mechanisms have also been responsible for the presence of fine equiaxed grains with an abnormally high fraction of twin boundaries in additively manufactured parts made of Al-alloys [39], [40], or Ni-alloys [41], [42]. Those recent studies demonstrate that ISRO leads to grain refinement in those FCC metals in 3D printed parts. However, iQCs involved in the nucleation mechanism were never experimentally evidenced, and more importantly, the physical and chemical reasons possibly accounting for the activation of such a nucleation mechanism were not discussed. Achieving an in-depth understanding of the underlying reasons promoting or on the contrary inhibiting ISRO in the liquid is yet of great interest if one aims at fully exploiting the microstructural capabilities offered by ISRO-based mechanisms while designing alloys for additive manufacturing.

To investigate the possible relation and impact of the grain microstructure, we perform a multi-scale microstructural study from the grain scale down to the nanoscale of a novel Al-alloy containing additions like Mn and Zr designed for and fabricated via L-PBF. For that purpose, we have associated transmission electron microscopy (TEM), namely Automated The rationale behind the choice of such alloying system can be found in [39]. Crystal Orientation Mapping (ACOM) an advanced technique able to perform in-depth crystallographic analyses at the nano-scale, and X-ray synchrotron nano-tomography allowing to finely characterize the microstructure in 3D. Such a combination of techniques is appropriate to reveal crucial information on the microstructure inherited from L-PBF that was not available to date. The consequences of ISRO on the microstructure inherited from additive manufacturing are further discussed highlighting various positive effects. We finally suggest that promoting ISRO in the liquid should be considered a new and promising alloy design strategy in the framework of additive manufacturing.

2. Experimental Procedures

2.1. Materials and processing conditions

The material investigated is a new Al-4Mn-3Ni-2Cu-1Zr alloy designed for L-PBF. The chemical composition of the as-received powder, measured by inductively coupled plasma atomic emission spectroscopy (ICP-AES) analysis, is given in **Table 1**. Pre-alloyed powder with a size distribution between 10 and 70 µm was gas atomized. Powder particles showed a spherical morphology with some satellites, see micrograph provided in supplementary materials in **Figure S 1**. Cylindrical samples with an 11 mm diameter and a height of 60 mm were fabricated in an EOS M290 L-PBF machine equipped with a Gaussian 400 W fiber laser (spot size of 80 µm) in a high purity argon environment (0.2% O_2). A laser power of 370 W, a laser scan speed of 1600 mm/s, a hatching distance of 140 µm (h), and a layer thickness of 60 µm (e) were used to build the cylindrical specimens. The scan strategy consists of 4 mm stripes and bi-directional scanning with a 67° rotation between consecutive layers. The building substrate temperature was held at 100°C throughout the builds.

Al	Mn	Ni	Cu	Zr
Bal.	3.87	3.14	1.86	1.02

Table 1 : Chemical composition is given in %.wt of the pre-alloyed powder batch used in the present work.

A Zr-free version of this alloy was also investigated in this work for comparison. Samples were produced in the same conditions (P = 370 W, v = 1600 mm/s, spot size = 80 µm) using the same scanning strategy and the same machine (EOS M290).

2.2. Microstructural characterization

The grain structure was characterized at different scales using an opto-numerical Olympus DSX500 microscope and a Zeiss Gemini SEM 500 FEG equipped with an Electron Backscattered Diffraction (EBSD) detector. Samples were mechanically ground using SiC abrasive papers down to the P4000 grade followed by a polishing step with a 1µm-diamond suspension. A final vibratory polishing using a 0.03 µm colloidal silica solution was performed using the VibroMet device from Buehler. Large EBSD maps were collected to obtain crystallographic information on the FCC-Al grains. Regarding grain morphology, a grain sphericity index Ψ was calculated from the following equation recently proposed in [43]: $\Psi = \frac{A}{P.R}$ where A is the grain area, P is the perimeter, and R is the equivalent radius of the matrix grains. Based on this sphericity index, equiaxed grains are defined as grains with $\Psi >$ 0.35 while others are considered columnar grains. The grain equivalent diameter was finally estimated from those EBSD maps, considering grains as spherical, with the following equation is: $D = 2(\frac{A}{\pi})^{1/2}$, where A is the area of the grain.

To investigate the microstructure at the micron scale, TEM has been carried out on thin foils prepared by electropolishing with a Tenupol 5 using a solution consisting of 20% Nitric acid 80% methanol at -30°C, and 15V. Site-specific lift-outs using a Focused Ion Beam (Zeiss NVision 40 Ga FIB-SEM) were performed to extract lamellae from a specific region of interest. First, a 1 µm-thick lamella protected by carbon and platinum (total thickness 1 µm) was extracted from the bulk. Successive Ga milling was employed to reduce the thickness of the lamella to less than 100 nm. The final thinning steps were carried out on both sides of the lamella at an accelerating voltage of 30kV with a probe current of 40 pA and 0.8° grazing angles.

ACOM (Automated Crystallographic Orientation Mapping) was performed with the hardware and software toolset ASTAR™ from Nanomegas. More details regarding this technique can be found in [44]. To summarize, a nano-beam is scanned over the area of interest. At each point of the scan, diffraction patterns are recorded with a CCD camera. By post-processing the diffraction data set, the phase and orientation at each position are assigned by comparing the experimental diffraction patterns to the theoretical ones of candidate phases using a template matching technique. Note that ACOM only establishes correlations between acquired and simulated patterns, thus it is crucial to preliminarily established a list of candidate phases. The list of candidate phases was established based on X-ray diffraction analyses and thermodynamic calculations, see [45], [46] for more details. The quality of the matching between experimental and theoretical patterns is evaluated by two indices: correlation index I and phase or orientation reliability R. The correlation index (I) measures the correlation between the experimentally recorded pattern and the theoretical template of a given phase. The simulated pattern having the highest correlation index with the experimental diffraction pattern gives the best solution. The phase/orientation reliability index R is sometimes overlaid on the patterns and is defined as R = $100(1 - I_1/I_2)$ I_1 and I_2 being the correlation indices of the two best solutions for respectively the candidate phase and orientation. When this parameter R is above 15, the identified phase is by far the best solution out of all candidates [44].

3D microstructure determination was carried out at the European synchrotron-ESRF using nano-CT on the beamline ID16B [47]. The X-ray beam of 29.6 keV was focused into a nanobeam (50×50 nm^2), using a Kirkpatrick-Baez (KB) pair of mirrors. The focused beam acts as a secondary source producing a conic beam. The camera, a PCO Edge 5.5 Camera link CMOS (2560×2160 pixels), was placed downstream at a fixed distance from the secondary source. Hence, by adjusting the sample position between the secondary source and the detector, different fields of view and consequently different magnifications can be chosen. For those measurements, an effective pixel size of 0.025×0.025 μm^2 was set. Objects smaller than 50 nm cannot be resolved properly. The technique used is in-line X-ray holotomography based on phase contrast imaging [48], each nano-holotomographic scan consists of four tomographic scans at slightly different propagation distances between the sample and the detector for each scan. For each scan, 4995 projections with an acquisition time of 0.05s per projection were acquired over 360°. The limitations of the camera field of view (FOV) were artificially increased: (i) horizontally by using the so-called half-acquisition method with

a position offset of the rotation axis of 700 pixels (over 2560), (ii) vertically by concatenating four tomographic scans acquired on top of each other along the vertical axis of the sample with a FOV overlap of 400 pixels. From the aligned raw images, phase contrast was retrieved using an algorithm based on the Contrast Transfer function method. The final volume of 99 x 99 x 200 μm^3 was reconstructed from those phase images using filtered back projection with the ESRF software PyHST2 [49].

2.3. Thermodynamic calculations

Thermodynamic solidification calculations were conducted using Thermo-Calc with the database dedicated to Al-alloys (TCAL6 version 6.0). Calculations were run using the Scheil-Gulliver model by considering only phases that have been identified experimentally in a previous study: Al_9Ni_2, $Al_{60}Mn_{11}Ni_4$, Al_3Ni_2, or Al_2Cu [39]. Note that the $Al_{60}Mn_{11}Ni_4$ phase (Pearson's crystal database) is described in the TCAL6 database as the $Al_{31}Mn_6Ni_2$ phase (orthorhombic phase). Both descriptions correspond to the same orthorhombic phase. In the Scheil-Gulliver model, it is assumed infinite diffusion in the liquid, no diffusion in the solid, and equilibrium at the solid/liquid interface. We are aware that the Scheil-Gulliver model suffers from several limitations with respect to the L-PBF processing conditions. For example, it neglects solute trapping although it can play a key role in the solidification sequence.

3. Experimental Results

3.1. Materials integrity at the nanoscale

Figure 1(a) gives an overview of the microstructure. Some spherical pores with an average equivalent diameter of nearly 10 µm are observed, see yellow arrows in **Figure 1**(a). **Figure 1**(b) proves the possibility to print near fully dense parts without cracks and with a very limited content of porosity (0.03% based on X-ray nano-CT scans). There are two populations of defects: the larger ones with a rather spherical morphology while the smaller ones are more tortuous. Owing to the high resolution of nano-CT, the morphological details of those tortuous pores extending over 3 µm are identified. Based on **Figure 1**(c), the characteristic size of tortuous pores is about 500 nm, which is very small compared to the ten-micron-sized spherical ones. According to the 3D nano-imaging experiment (see 2D cross-sections), which allows the revealing of the microstructure and defects, the tortuous pores are exclusively found in the interdendritic regions. Finally, such tortuous pores can lie only 1 µm away from one another and seem to be separated by intermetallics. The mechanism responsible for the presence of those tortuous pores is believed to be insufficient liquid feeding. Those pores can thus be classified as microshrinkages.

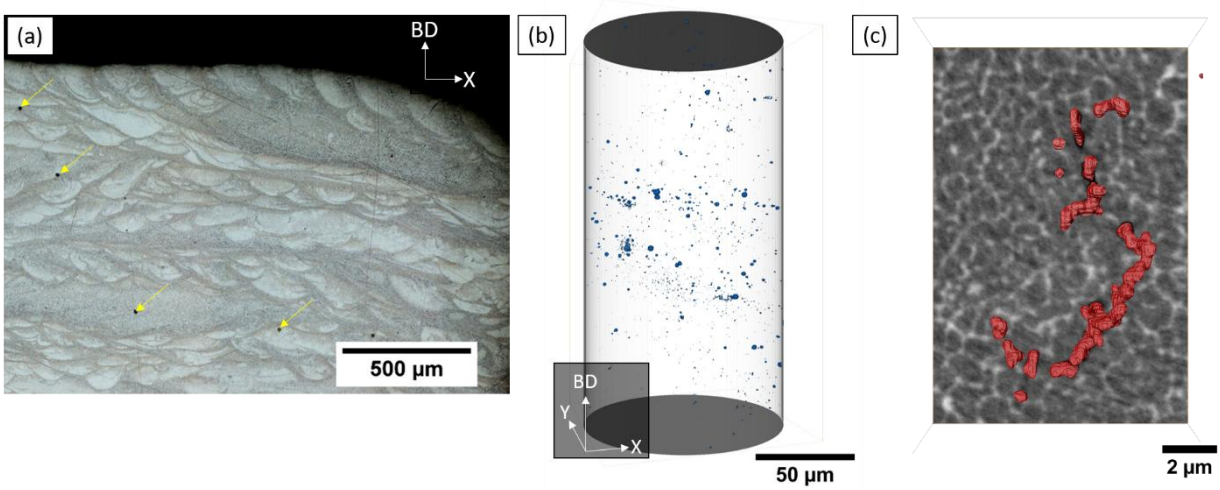

Figure 1: (a) Optical micrograph of a crack-free sample after chemical etching using Keller's reagent. The yellow arrows point out some spherical pores. (b) 3D rendering of the defect population as revealed by nano-XCT with a 25 nm voxel size for better visualization of the two populations of pores. (c) A 3D view of small tortuous pores in red superimposed on a 2D cross-section to show its position within the microstructure. Intermetallics are displayed in bright contrast while the matrix appears in dark contrast.

3.2 A complex multiscale microstructure

The EBSD map in **Figure 2**(a) is characterized by a region that can be indexed representing about 60 % of the surface while the black regions are associated with unreliable indexing regions. Those regions are located mostly along the melt pool boundaries and locally inside the melt pools (see the magenta arrow in **Figure 2**(a)). The indexed zones contain both micron-sized columnar grains and coarse equiaxed grains as illustrated in **Figure 2**(a). Therefore, in the following, they will be qualified as near columnar zones (NCZ). The NCZ is mostly found in the center and at the top of the melt pool, see **Figure 2**(a). It also reveals two kinds of dendritic growth morphologies: a classical columnar one (see white arrow in **Figure 2**(b)), and a feathery one (see yellow arrow in **Figure 2**(b)). Finally, according to the EBSD map, the NCZ shows a weak crystallographic texture (**Figure S 1**).

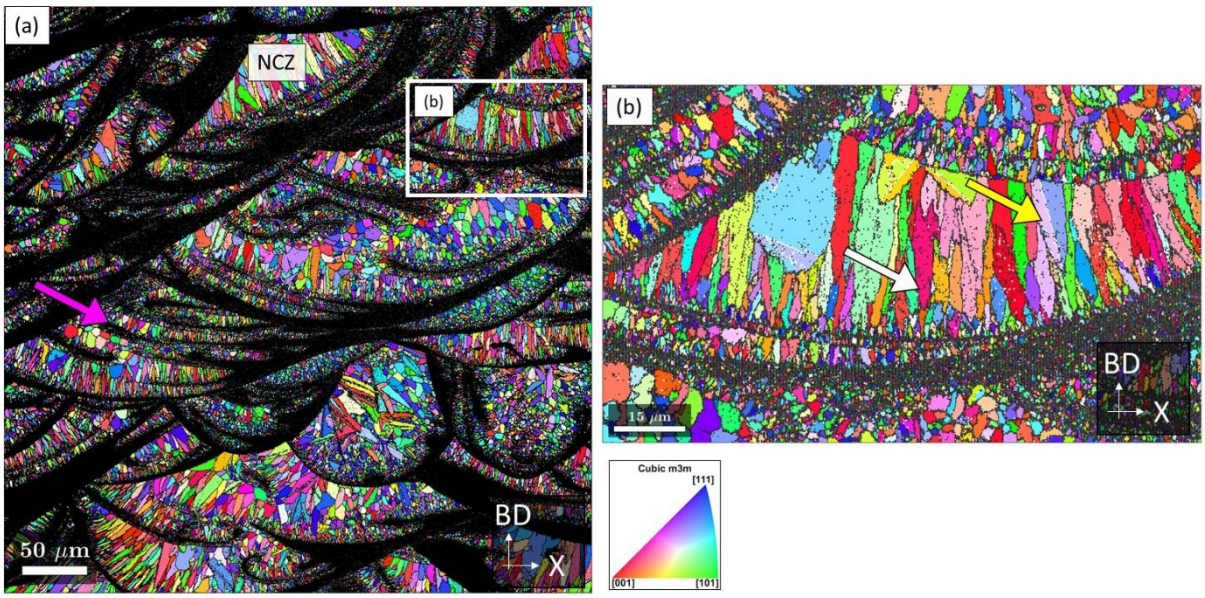

Figure 2: (a) IPF-EBSD map acquired in a plane containing the Building Direction (BD) (200 nm step size). Only aluminum grains were indexed. (b)Enlarged view of a melt pool inside the NCZ corresponding to the white square box shown in (a). Two growth morphologies are revealed: the classic cellular one (white arrow) and the feathery one (yellow arrow). The magenta arrow in (a) indicates that the unindexed regions could be observed at the melt pool center because of convection flows in the liquid.

Regarding the black regions in **Figure 2**(a), the step size of the EBSD mapping being 200 nm, the presence of submicronic grains along with a high density of grain boundaries decorated with a high fraction of intermetallics can explain the absence of reliable indexing. A high-resolution study is necessary to investigate at a fine scale the microstructure in such unindexed regions. This has been performed using the ACOM (Automated Crystallographic Orientation Mapping) method.

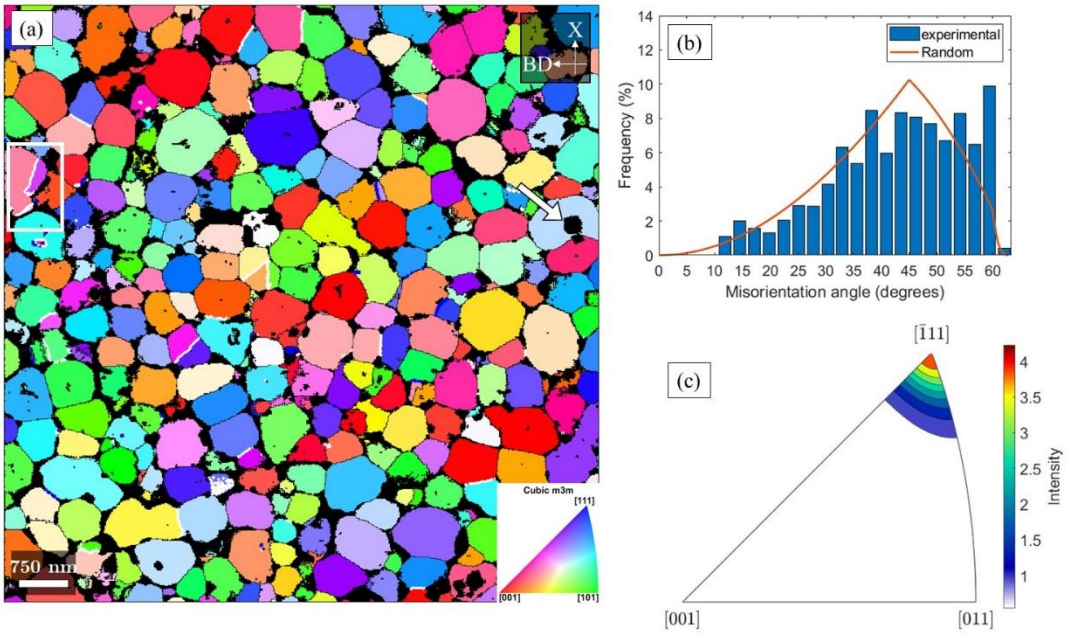

Figure 3: (a) Crystallographic orientation maps (IPF) for FCC-Aluminum acquired in a Fine Equiaxed Zone (FEZ) using ACOM (15 nm step size). Σ3 orientation relationships are highlighted in white. Intermetallics are displayed in black. (b) Misorientation distribution within the region of interest shown in (a), and (c) rotation axis distribution considering only boundaries with a misorientation angle between 58° and 62°.

Figure 3(a) presents a high-resolution orientation map obtained using ACOM. This map reveals a microstructure consisting of submicronic aluminum grains separated by phases characterized by large lattice parameters typical of intermetallic phases. The aluminum grains have a mean grain size estimated to be about 610 ± 250 nm (see **Figure S 3** for the grain size distribution). In the Fine Equiaxed Zone (FEZ), aluminum grains do not show a particular texture. The intermetallic phase fraction derived from **Figure 3**(a) and from the 3D reconstructed volume obtained by nano-XCT, is about 35 ± 4%. There are two populations of intermetallics depending on their spatial distribution. Those located in the interdendritic spaces have been identified by nano diffraction as Al_9Ni_2, $Al_{60}Mn_{11}Ni_4$, Al_3Ni_2, or Al_2Cu in a previous study [39]. Those located in the center of grains have been mostly identified as primary Al_3Zr (see **Figure S 2**). Besides, the cube-cube orientation relationship confirms the epitaxial nucleation of matrix grains from the primary Al_3Zr precipitates, see **Figure S 2**(b-d)).

Considering only grain boundaries, **Figure 3**(b) indicates a high frequency of the 60° misorientation angle in comparison with the random distribution (e.g. Mackenzie distribution). Regarding now the rotation axis for grain boundaries with a misorientation angle equal to $60 \pm 2°$, the IPF-map in **Figure 3**(c) reveals an intense peak close to the <111> direction. This can be seen as a signature of the presence of twin relationships. These observations made on a small region of interest show a high density of Σ3 boundaries in this alloy (see white lines in **Figure 3**(a)). The fraction of Σ3 specific boundaries is estimated as follows: $\%\Sigma_3 = \frac{L_{\Sigma_3}}{L_{tot}}$, where $L_{\Sigma 3}$ is the total length of Σ3 boundaries and L_{tot} is the total length of grains boundaries. **Figure 3**(a) highlights a large proportion of Σ3 boundaries, about 3.5% considering a 2° tolerance for the misorientation angle (it is only 0.13% in a random population of grains when considering a 5° tolerance). The Σ3 boundaries are frequently referred to as twin boundaries. Indeed, in the present case, the term twin boundary does not necessarily seem appropriate because the aluminum grains frequently appear separated by intermetallic phases. This is why the microstructure has been here analyzed using the rotation angle and rotation axis. This approach has revealed that a specific feature of the FEZ was to have a high density of grains with a Σ3 orientation relationship. Σ3 boundaries are not expected in microstructures of Al-alloys inherited from solidification because the stacking fault energy is relatively high in aluminum alloys [50]–[53] even in presence of alloying elements. Even though some studies report the possibility to create twin boundaries during deformation in presence of ultra-fine grains, we could find no reason why the Σ3 boundaries observed here could result from a deformation mechanism.

3.3. Local crystallographic analyses

For a better understanding of the mechanism responsible for the Σ3 (or twin) boundaries, two local crystallographic analyses are performed in the FEZ. The first study considers a cluster of six grains in a very close neighborhood, and the second one takes into account two matrix grains around a particle identified as the $Al_{60}Mn_{11}Ni_4$ phase.

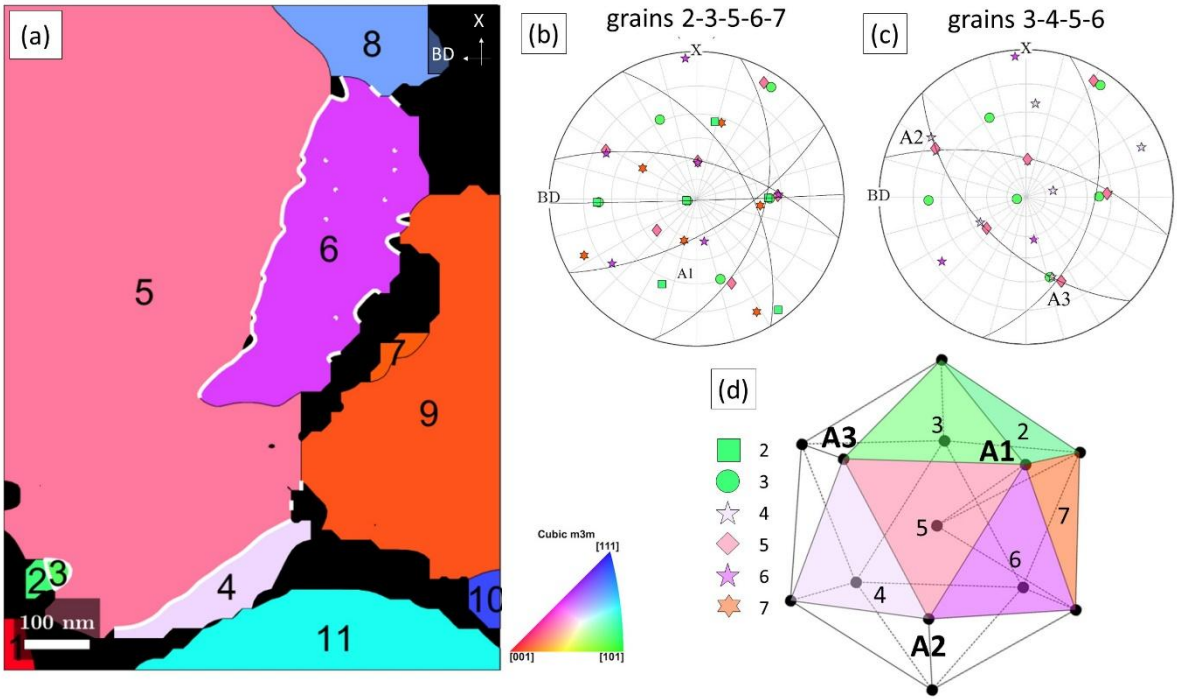

Figure 4 : (a) Enlarged view of the selected area highlighted in the orientation map shown in Figure 3(a). The color code in Figure 4(a) is associated with the grain crystallographic orientation of the FCC Al phase and will be further used in Figures 4 (b), (c), and (d). Intermetallic phases in the interdendritic spaces are displayed in black, while twin boundaries identified by an automatic analysis are drawn in white. Stereographic projection showing the <110> directions for (b) grains 2-3-5-6-7 and (c) grains 3-4-5-6. Figure 4(b) shows that one <110> direction labelled A1 is common to the five grains 2-3-5-6-7) and several are common to two grains. A mirror symmetry is also related grains 2 and 3, grains 3 and 5, grains 5 and 6, and grains 7 and 2. For each pair of grains, the mirror plane is close to the (111) plane indicated by the black meridian. Note that the 5 mirror planes almost intersect at the <110> direction shared by the five grains. They are related by a rotation of nearly 36° around the common <110> direction shared, characteristic of a 5-fold symmetry. Figure 4(b) shows that for grains 3-4-5-6, there are <110> directions common to two grains related by a mirror symmetry. The <110> direction common to grains 3-5-6 corresponds to the 5-fold axis identified in Figure 4 (b) and labelled A1 while the stereographic projection shows that the directions common to grains 4-5-6 and 3-5-6 (respectively labelled A2 and A3) are consistent with other 5-fold axes of the icosahedral symmetry. (d) Schematic representation of the mutual orientation relations of the six grains (2 to 7) based on a hypothetical icosahedral nucleus. The directions common to several grains labelled A1, A2 and A3 have been also reported.

The ACOM orientation map in **Figure 4**(a) shows a region of interest with a cluster of grains, where both phases and grain boundaries are present. The automatic crystallographic analysis has shown that numerous grains are related two-by-two by a Σ3 orientation relationship and that among the grain boundaries, most of them can be identified as twins (see white lines).

The stereographic projection given in **Figure 4**(b) that displays the <110> directions of the grains 2 to 7 labelled in **Figure 4**(a) reveals many common directions between these grains. The crystallographic analysis shows that the mirror planes between grains 2 and 3, grains 3 and 5, grans 5 and 6, and grains 7 and 2 correspond to the (111) plane which demonstrates the existence of Σ3 twin relationships. Also, there is a <110>-direction common to these five grains. This common <110>-direction (labelled A1 in **Figure 4**(b)) corresponds to the intersection of the twin planes of the grains which are related by a

rotation of about 72° along this common axis. The direction labelled A1 in **Figure 4***(*b) is thus a fivefold symmetry axis between grains 2, 3, 5, 6, and 7. In addition, the relation between grains 6 and 7 corresponds to a 60° rotation around the <111>-direction and a 7° rotation around <110>, known as a near-twin relationship. This corresponds to the deficiency gap resulting from the construction of the icosahedron from 20 tetrahedra where facets are {111}-planes, see [37].

Following the same approach, the relations between grains 3-4-5, and between grains 4-5-6 (see **Figure 4***(*c)) have been analyzed. It was concluded that the grains have in common two other <110> directions respectively labelled A2 and A3 in **Figure 4***(*d) whose orientations are consistent with two other 5-fold axes of an icosahedron (see **Figure 4** captions for more details). As summarized in the schematic given in **Figure 4**(d), the cluster of grains exhibits more than a single 5-fold symmetry axis as one may reconstruct a hypothetical icosahedron that is thought to be responsible for the high density of Σ3 boundaries or twin relationships between these grains. This observation led us to propose a hypothetical icosahedral template acting as a nucleus for the investigated cluster of aluminum grains, see **Figure 4***(*d). This point of view has already been invoked for other aluminum alloys manufactured by more traditional casting routes to account for the unexpected presence of a high density of Σ3 boundaries [37]. However, additional observations of the microstructure in the FEZ possibly related to the mechanisms involved in the nucleation of the FCC-Al grains have been collected and are presented hereafter.

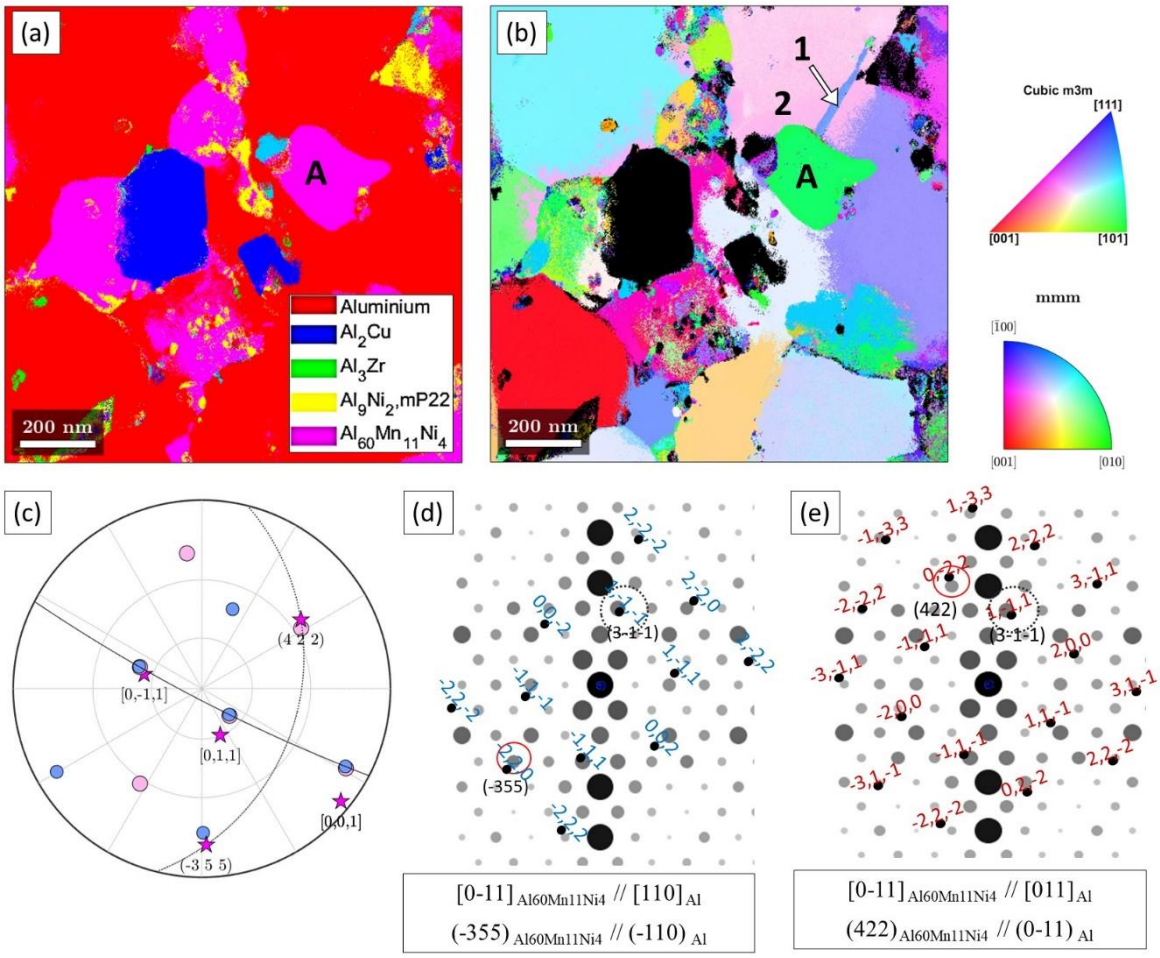

Figure 5: (a) ACOM Phase map acquired in the FEZ (2 nm step size) in a FIB lamella showing the presence of a lot of intermetallic phases. (b) ACOM orientation map for Al and $Al_{60}Mn_{11}Ni_4$. (c) Stereographic projection of the <110> direction for grains 1 (blue circle) and 2 (pink circle) superimposed with some simple directions of the $Al_{60}Mn_{11}Ni_4$ phase (magenta star). The planes (-355) and (422) (magenta star) have been found using an automatic search on the ACOM indexed data to be close to <110> Al directions respectively belonging to grain 1 and grain 2. The resulting orientation relationship between the $Al_{60}Mn_{11}Ni_4$ particle A and grain 1 and grain 2 respectively are given in the black frames. In agreement with these

relationships, the diffraction patterns have been simulated for the $Al_{60}Mn_{11}Ni_4$ particle A and grain 1 (d) (respectively grain 2 in (e)). The red circles correspond to the proximity identified by the automatic search. In both cases (d), (e), as marked by the dotted circles a correspondence with a good matching is observed between the planes (1 -1 1) in Al and the (3 -1 -1) in $Al_{60}Mn_{11}Ni_4$ ($d_{1-11,Al} = 0.234\ nm$ almost equal to $d_{3-1-1,Al60Mn11Ni4} = 0.245\ nm$).

The most frequent intermetallic phases have been identified by ACOM as the $Al_{60}Mn_{11}Ni_4$ phase. Since this complex phase can nucleate before the Aluminum matrix as shown by thermodynamic calculations (**Figure S 5**), it can be considered a primary phase. **Figure 5**(b) evidences Aluminum equiaxed grains and $Al_{60}Mn_{11}Ni_4$ phase particles with well-identified orientations, i.e. without high internal orientation variations (see grain labelled A). According to the automated analysis, in the vicinity of this $Al_{60}Mn_{11}Ni_4$ grain A, there are two adjacent aluminum grains (labelled 1 and 2 in **Figure 5**(b)) related by a twin relationship. Considering the specific relevance of twins in the present alloy, the orientation relationship of Aluminum and $Al_{60}Mn_{11}Ni_4$ grains (respectively labelled 1, 2, and A) were more deeply analyzed.

The stereographic projection shown in **Figure 5**(c) reveals that the two aluminum grains share three <110> directions and have a 60° misorientation angle, proving that they are in a twin relationship (see black line in **Figure 5**(c) corresponding to the twin plane). In addition, the [0 -11] direction of the $Al_{60}Mn_{11}Ni_4$ phase is aligned with one of the shared <110> Al directions of the two matrix grains. The other shared <110> Al directions of the two aluminum grains, and laying in the twin plane, also appear rather close to the [0-11] and [001] directions of the $Al_{60}Mn_{11}Ni_4$ phase. Considering the high proximity observed between the shared <110> Al direction and the [-110] direction of the $Al_{60}Mn_{11}Ni_4$ phase, this orientation has been analyzed in more detail.

From the orientation map displayed in **Figure 5**(c), the orientation relationship between grain 1, grain 2, and the $Al_{60}Mn_{11}Ni_4$ particle labelled A has been derived using an automatic search of the closest directions between particle A and respectively grain 1 and grain 2. The following relations have been respectively determined from the simulated diffraction patterns:

$$[0\text{-}11]_{Al60Mn11Ni4} \,//\, [110]_{Al} \text{ and } (\text{-}355)_{Al60Mn11Ni4} \,//\, (\text{-}110)_{Al}$$

$$[0\text{-}11]_{Al60Mn11Ni4} \,//\, [011]_{Al} \text{ and } (422)_{Al60Mn11Ni4} \,//\, (0\text{-}11)_{Al}$$

Those simulated diffraction patterns (**Figure 5**(d) and (e)) have been further used to examine the matching between the $Al_{60}Mn_{11}Ni_4$ particle labelled A, and the two matrix grains, namely grain 1 and grain 2.

Figure 5(d-e) displays the overlapping of the simulated diffraction pattern: for grain 1 and particle A on the left, and for grain 2 and particle A on the right. Remarkably for both grains, the same matching is observed between the (1 -1 1) in Al planes and the (3 -1 -1) planes of the $Al_{60}Mn_{11}Ni_4$ particle A. Consequently, not only there is a good matching between the $Al_{60}Mn_{11}Ni_4$ particle A and the Aluminum grains but the two relationships described above correspond to the same orientation relationships. In other words, grain 1 and grain 2 are variants of the same orientation relationship between the $Al_{60}Mn_{11}Ni_4$ and the Aluminum. It means that the $Al_{60}Mn_{11}Ni_4$ particle A is the parent phase and that two variants have been found to nucleate from it. It finally means that the twin boundaries which are not expected in aluminum alloys as reminded above are also resulting from the heterogeneous nucleation of aluminum grains on the $Al_{60}Mn_{11}Ni_4$ primary phase.

3.4. Twin Dendrites: Morphology and Growth direction

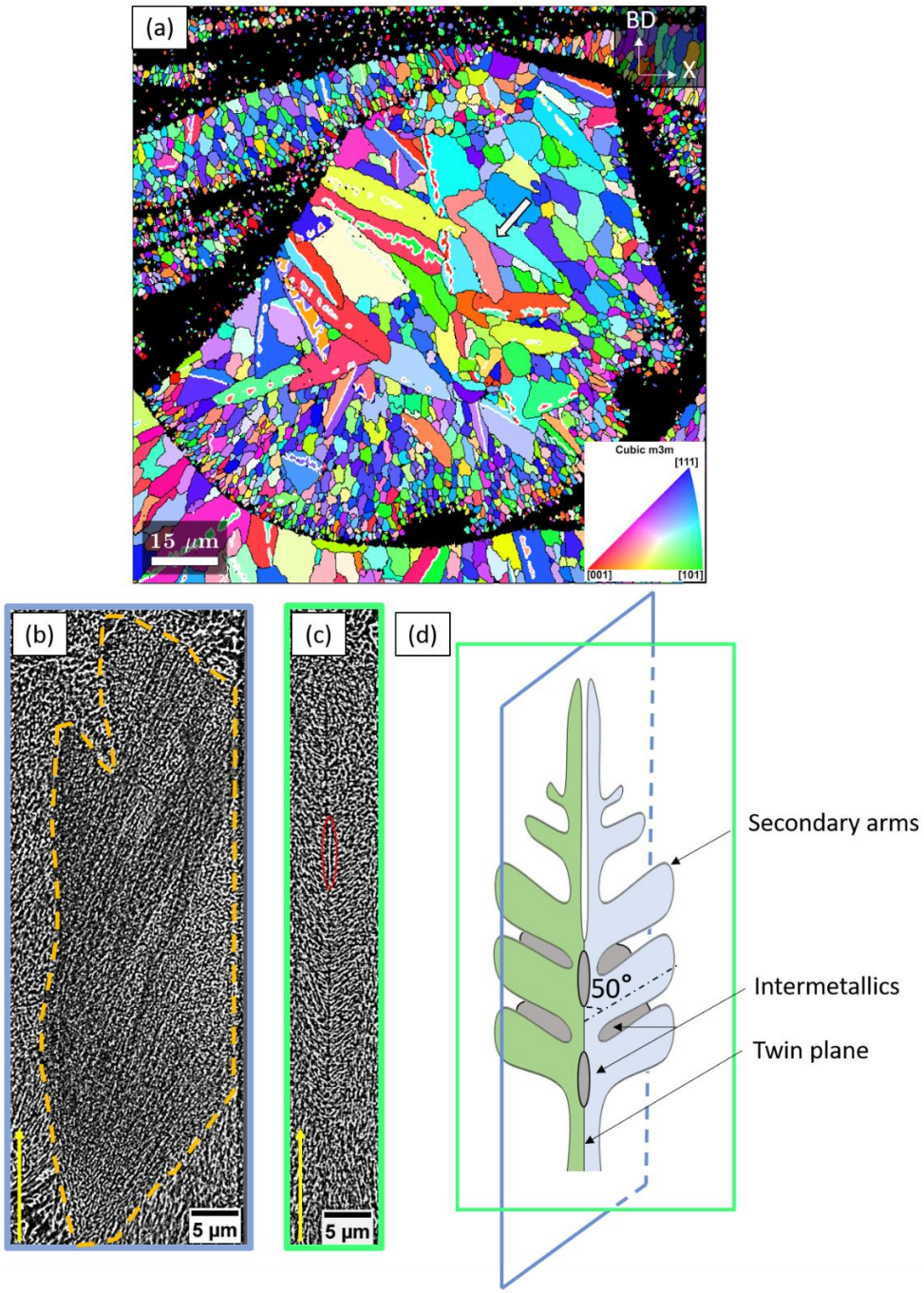

Figure 6: (a) IPF-EBSD map of the matrix orientation with the finest grains in the FEZ appearing in black and Σ3 boundaries in white. 2D cross-sections extracted from the nano-CT 3D reconstruction where intermetallics appear in bright and the matrix in dark. (b) 2D cross-section extracted right at the twin plane that reveals the feather-like morphology of the twin dendrite. Orange dashed lines highlight the contours of this twin dendrite in the twin plane. (c) 2D cross-section taken perpendicularly from the view given in (b) for the same twin dendrite (view perpendicular to the twin plane and parallel to the Building Direction). It allows the observation of the secondary arms of the twin dendrite. The red ellipsoid points out intermetallics distributed along the twin plane. The building direction is indicated with a yellow arrow. (e) Schematic representation of a feathery grain to illustrate the morphology of the twin dendrite observed in (c), the distribution of intermetallics, and the angle between the trunk and the secondary arms.

Figure 6(a) shows an IPF orientation map in the NCZ with identified twin grains since most are split into two sides by a twin plane (see white lines). The proportion of grain boundaries in a twin relationship is 5% which is higher than in the FEZ. To get a detailed description of the dendrite morphology and size, one requires a 3D characterization. We performed here synchrotron nano-XCT (voxel size 25 nm). **Figure 6**(b) and **Figure 6**(c) show two different 2D cross-sections extracted from the 3D reconstructed image in specific planes. **Figure 6**(b) is taken in the twin plane that can be easily identifiable based on the variation of contrast at the twin plane. The dashed lines confirm the typical feather-like morphology of the twin dendrite observed in EBSD (see grain pointed out with a white arrow in **Figure 6**(a)). This twin dendrite is well-developed since its width is about 10 µm. **Figure 6**(c) is a 2D cross-section taken perpendicularly to the twin plane and reveals the presence of secondary arms, a situation contrasting with most of the microstructures inherited from L-PBF where the development of secondary arms is often very limited. From **Figure 6**(c), the angle between the trunk and the arms was estimated to be roughly 50°. Finally, the red ellipsoid in **Figure 6**(c) points out intermetallics distributed along the twin plane with the same morphology as those observed in the interdendritic spaces. **Figure 6**(d) gives a schematic 3D view of the feathery morphology of twin dendrites.

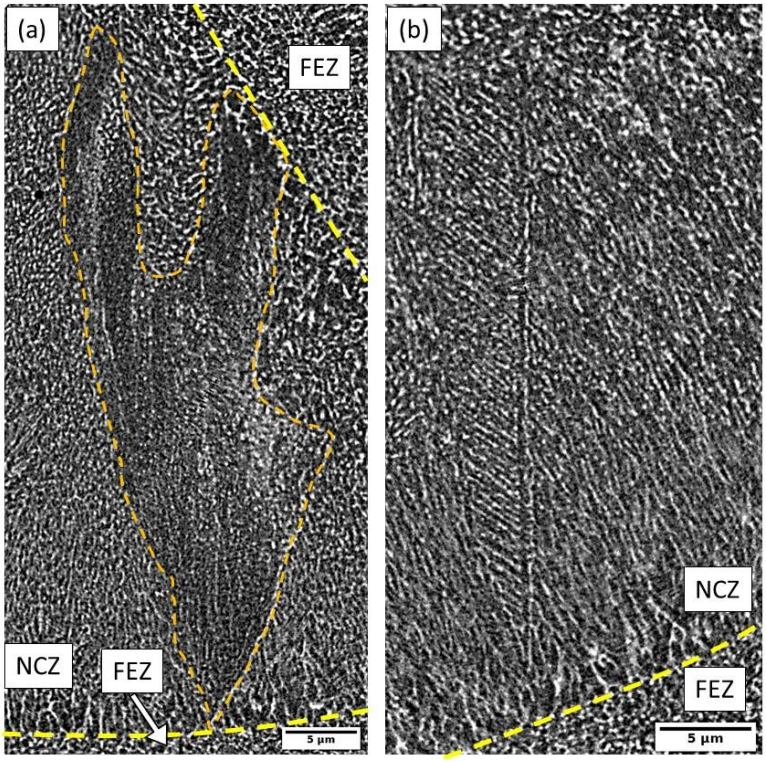

Figure 7 : 2D cross-section extracted from the reconstructed 3D image based on Nano-XCT and showing a transition between the FEZ and the NCZ (building direction is aligned vertically). Two different views of a twin dendrite: (a) view parallel to the twin plane; (b) view perpendicular to the twin plane. The orange dashed line shows the contours of the twin dendrite and the yellow dashed line represents the boundary between the FEZ and the NCZ.

Finally, 2D cross-sections extracted from the 3D reconstruction of the microstructure suggest that twin dendrites nucleate from the FEZ, see **Figure 7**(a-b). However, the twin dendrite growth direction could not be determined from nano-XCT images. As a result, another region of interest containing a twin dendrite was selected and characterized using ACOM, see **Figure 8**.

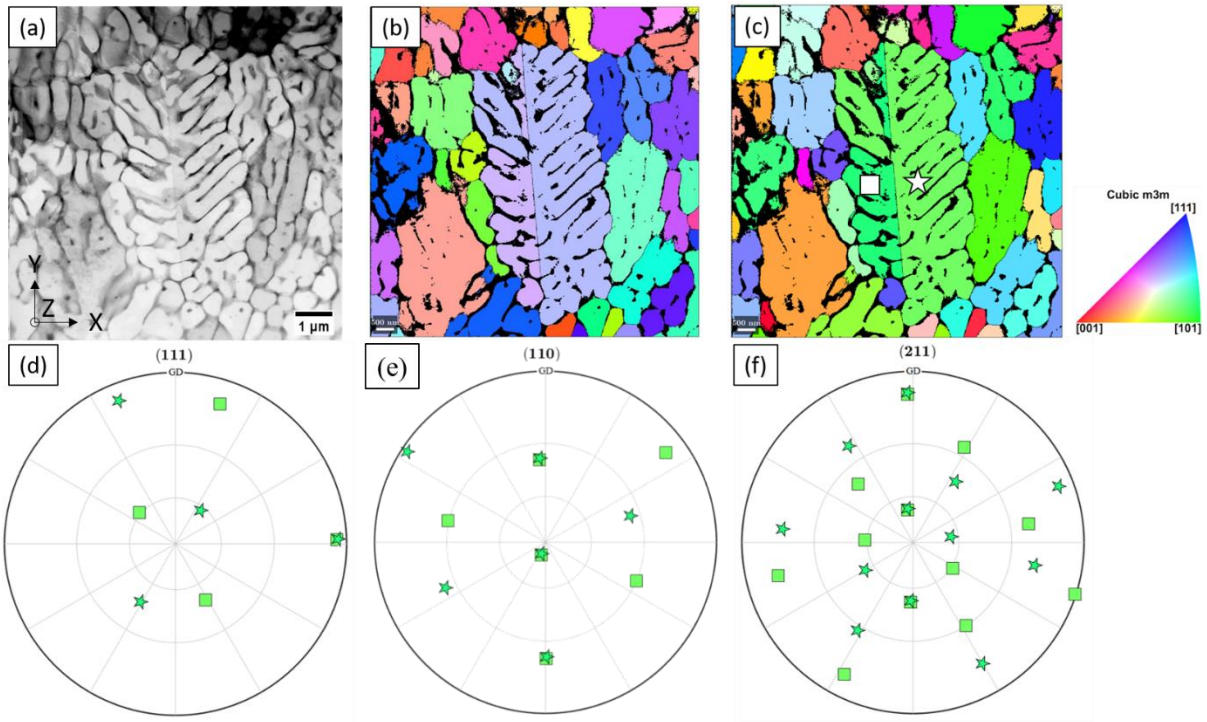

Figure 8 : Orientation study of an electropolished TEM lamella extracted parallel to the building direction. (a) Virtual Bright Field image of a twin dendrite. ACOM IPF maps two normal in-plane directions: (b) z-direction, (c) y-direction. The left side of the dendrite is represented by a square symbol and the other side by a circle one as suggested shown in (c). For the two sides of these dendrites, pole figures of various planes are plotted in(d) (111), (e) (110), and (f) (112).

Figure 8(a) shows a region of interest containing a twin dendrite. The two sides of the twin dendrites have a similar crystallographic orientation color in **Figure 8**(b-c). According to **Figure 8**(d-e), the twin dendrite is indeed seen as schematically shown in **Figure 6**(d): the growth direction is in the lamella plane and points upwards along a <112> direction as indicated by the pole figure shown in **Figure 8**(f). **Figure 8**(a) also confirms the 50° angle between the primary trunk and secondary arms, previously measured on the 2D cross-section, see **Figure 6**(c). Finally, since the growth direction of the trunk is a <112> direction and the arms are in the lamella plane, this 50° angle between the trunk and arms proves that arms grow along a <110> direction **Figure 8**(d) and (e).

4. Discussion

4.1. Grain refinement mechanisms

We have shown that the Al-Mn-Ni-Cu-Zr alloy studied here exhibits a very fine equiaxed zone with a mean grain size roughly equal to 600 nm. While the presence of such fine grains was already many times reported in different Al alloys designed for L-PBF (e.g. [19]–[23]), it should be emphasized that such fine grains in Al-alloys are usually achieved using severe plastic deformation. In addition, 3.5% of the grain boundaries have been found to correspond to Σ3 twin boundaries in the FEZ using a 2° tolerance for the misorientation angle. For comparison, even in the Al-Zn-Cr ternary alloy is reported as having a high frequency of Σ3 boundaries [54], a lower content of such boundaries was measured (only 2.3%, although using a higher tolerance for the misorientation angle). Clusters of equiaxed grains separated by Σ3 boundaries have also been recently observed in Inconel 718 [42] processed by direct energy deposition, and in an Al-alloy from the 7XXX-series modified with the addition of ZrH_2 [40] and fabricated by L-PBF.

Based on our experimental observations, we have identified three different nucleation mechanisms contributing to refining the grain size. Those three nucleation mechanisms are schematically summarized in **Figure 9**.

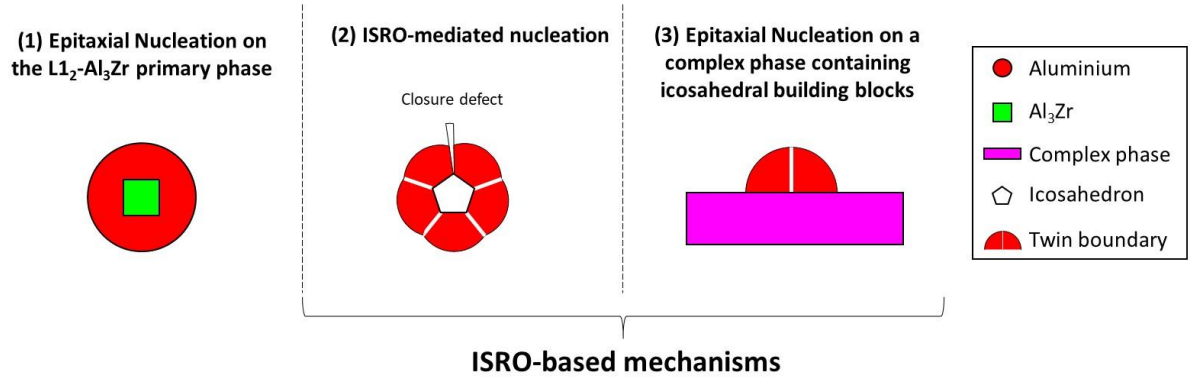

Figure 9 : The three nucleation mechanisms responsible for the Aluminum heterogeneous nucleation and the twin boundaries in the FEZ.

The first mechanism described hereafter as epitaxial nucleation on primary Al_3Zr phases is well-documented in the literature of AM Al-alloys (see e.g. [22], [24], [26]). Promoting epitaxial nucleation on the cubic primary phase Al_3X (X = Zr, Sc, Nb, or Er) is relatively straightforward as one needs to introduce a content of the X-solute beyond the peritectic limit [55]. Briefly, heterogeneous nucleation on the Al_3Zr primary phase occurs via peritectic transformation and is promoted by the small misfit parameter between Aluminum and Al_3Zr. The cube-cube orientation relationship supported by **Figure S 4** shows that one Al_3Zr primary phase implies the nucleation of one single Aluminum grain. Such a mechanism cannot be invoked to account for the unexpectedly high density of Σ3 twin boundaries.

We think that two additional nucleation mechanisms are responsible for the fine grain size observed in our alloy and both are thought to be closely related to the presence of ISRO in the liquid.
Based on the thermodynamics calculations shown in **Figure S 5**, both the Al_3Zr phase and the complex $Al_{60}Mn_{11}Ni_4$ phase can be considered primary phases. We showed in **Figure 5**(a-b) that this complex primary phase containing many icosahedral motifs in its unit cell (see **Figure 10**(a)) can also act as heterogeneous nucleation sites for Aluminum grains. **Figure 10**(b-c) reveal, based on theoretical diffraction patterns, the presence of pseudo-fivefold symmetry axes. The orientation relationship between the primary $Al_{60}Mn_{11}Ni_4$ complex phase and Aluminium is determined in **Figure 5**(d-e). As a result of this orientation relationship, four aluminum grains related 2 by 2 by a twin boundary can possibly nucleate from this complex phase. Thus, this $Al_{60}Mn_{11}Ni_4$ primary complex phase offers the

possibility to nucleate more than one aluminium grain and can account for the presence of Σ3 twin boundaries in the FEZ. Heterogeneous nucleation of Aluminum on the $Al_{60}Mn_{11}Ni_4$ primary phase requires further discussion because of the specific features of its complex structure compared to simple structures like, for instance, the $L1_2$-Al_3Zr one. The local atom packing into the $Al_{60}Mn_{11}Ni_4$ phase, related to the presence of icosahedral motifs in its unit cell as shown **Figure 10**(a) in results in a reduction of the interfacial energy between the melt and the intermetallic [56], [57]. This likely helps the heterogeneous nucleation of Aluminum grains from this complex phase.

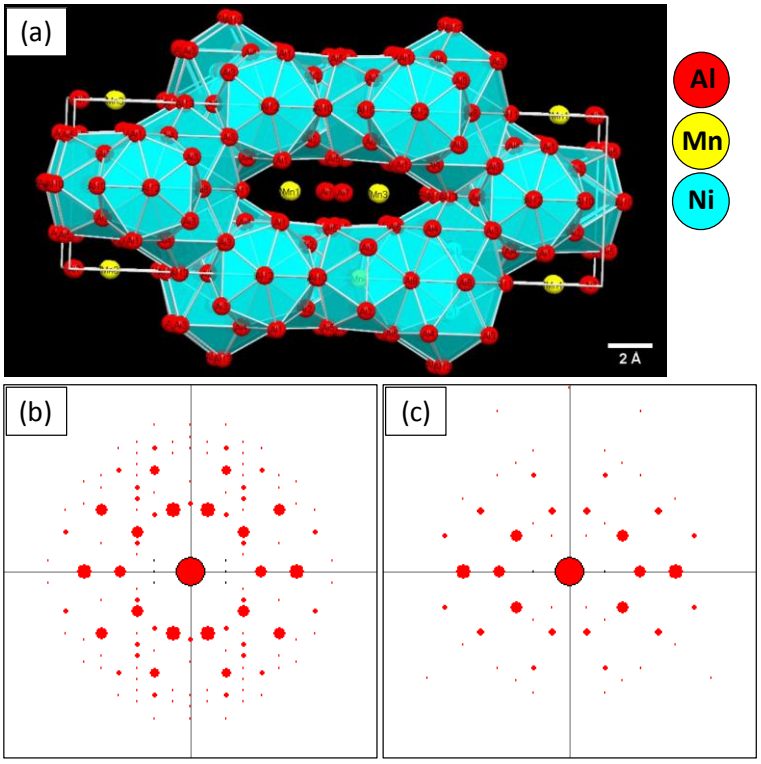

Figure 10 : (a) Icosahedral building blocks present in the $Al_{60}Mn_{11}Ni_4$ unit cell. The theoretical diffraction patterns of the: (b) [0 0 1] direction and (c) [0 1 1] direction revealing two pseudo-fivefold symmetry axes.

Interestingly, a high density of Σ3 twin boundaries has also been observed in regions in the FEZ where the complex primary phase was not found responsible for the nucleation of Al grains, see e.g. **Figure 4**(a). In this specific region of interest, the twinned aluminum grains form a cluster exhibiting three fivefold symmetry axes that can be described as an icosahedral template as shown in **Figure 4**(b-c). This mechanism has been identified as ISRO-mediated nucleation ([36], [38], [42], [54]) contributing to grain refinement in the FEZ and also explaining the unexpectedly high density of Σ3 twin boundaries found in the FEZ. ISRO-mediated nucleation occurs when the undercooling is high enough to promote a large proportion of ISRO into the liquid [58]. We think that ISRO-mediated nucleation requires larger undercooling in comparison to the nucleation mechanisms involving primary phases. Indeed, most aluminum grains in the FEZ likely nucleated before the critical undercooling for this third mechanism was reached. This idea was supported by the fact that finer grains seem to result from ISRO-mediated nucleation (**Figure 4**) compared to the Al grains nucleated from primary phases.

4.2. On the origin of twin dendrites

Interestingly, 3D images reconstructed based on the nano-XCT scan show that twin dendrites nucleate at the NCZ/FEZ boundaries as illustrated in **Figure 7**. The origin of twin dendrites has been

debated for years, yet the most convincing mechanism was proposed by Rappaz *et al.* in a recent viewpoint paper [36]. In Rappaz *et al.* [36], it is hypothesized that twin dendrites could nucleate via ISRO-mediated nucleation but only two nucleated grains from the icosahedral template would then be selected during the growth stage due to their proximity with the thermal gradient direction. As we have also evidenced the occurrence of two different nucleation mechanisms in the FEZ closely related to ISRO in the liquid, at first sight, we shared the point of view exposed in Rappaz *et al.* [36]. However, we would like to further discuss some details of their hypothesis that are related to specific features of the ISRO in metallic alloys.

As earlier demonstrated by Frank and Kasper [32], complex metallic alloys involving atoms of close size are characterized by local tetrahedral compact packing. In other words, the coordination polyhedra describing the local order around each atom are formed of equilateral triangles or slightly distorted ones. This is possible only for a limited number of polyhedra: the icosahedron and three related polyhedra called Z14, Z15, and Z16. The icosahedron, also called Z12, corresponds to a central atom surrounded by 12 neighbours. Z14, Z15, and Z16 environments correspond to a central atom surrounded by 14, 15, or 16 neighbours respectively. As illustrated in **Figure 11**(a-b), the icosahedron (Z12) is formed of 20 regular triangles all connected to 5-fold symmetry vertices while for the Z14 polyhedra, 12 triangles are slightly distorted and connected to 6-fold symmetry vertices. In complex metallic alloys, most atoms have a Z12 coordination number and larger atoms tend to have Z14, Z15, and Z16 coordination.

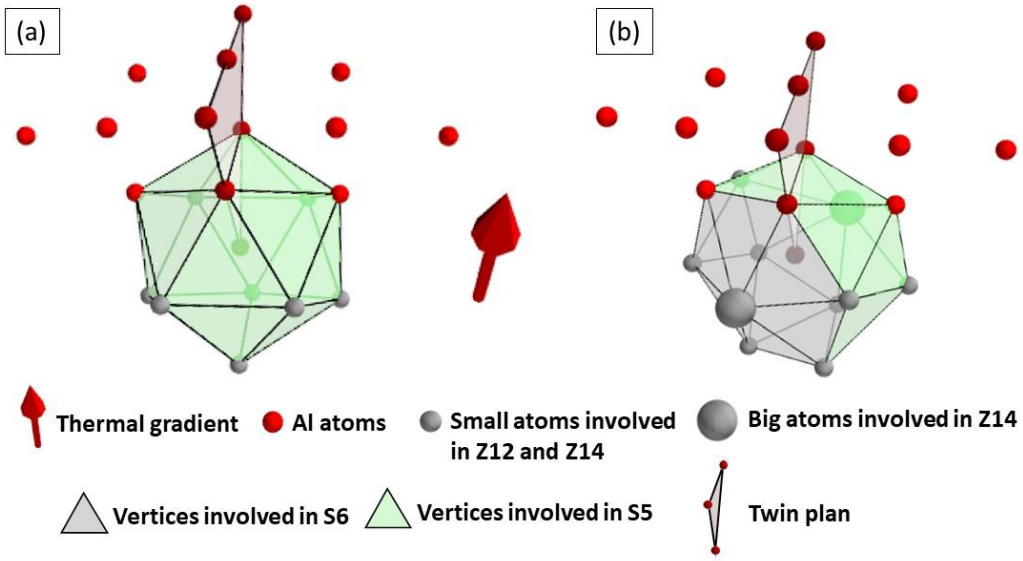

Figure 11: Schematic representation of the twin dendrite nucleation on (a) a Z12 environment (icosahedron) or (b) a Z14 environment. The green faces represent perfect tetrahedra which are thought to act as nucleation sites for twin dendrites while gray ones represent those that could not act as nucleation sites. Z15 and Z16 environments, not represented here, are similar to Z14 but with a higher degree of distortion (i.e. while the Z14 has two 6 fold vertices, Z15 et Z16 have three and four 6 fold vertices).

We would like first to highlight that icosahedral local ordering (Z12 coordination number) is the most isotropic local ordering in comparison with other kinds of local ordering with higher coordination numbers (Z14, Z15, or Z16) [32]. Thus, various twin dendrites could theoretically grow from an icosahedral template (Z12). Then, one should also keep in mind that icosahedral ordering (Z12) is often the predominant local ordering around Al atoms in liquid aluminium, see e.g. [59]. As a result, we would expect to observe many twin dendrites, some of them showing limited growth because not

necessarily aligned with the thermal gradient. On the contrary, the well-developed ones should be associated with those having their primary trunks parallel to the thermal gradient. However, our experimental observations rather reveal the presence of a few well-developed twin dendrites. If ISRO seems a reasonable hypothesis to account for the fine grain size and the unexpected presence of many Σ3 boundaries in the FEZ, we think that instead of the perfect icosahedral local ordering, other local orderings, still related to ISRO are worth considering to explain the formation of twin dendrites. To account for the development of twin dendrites, we suggest a mechanism slightly different from the one proposed by Rappaz *et al.* [36]. Indeed, instead of suggesting that twin dendrite nucleate from icosahedral local ordering (Z12), we rather propose that twin dendrite would rather nucleate from a Z14 local ordering as schematically shown in **Figure 11**(b). Our interpretation is supported by two ideas. The first idea is that icosahedral local ordering (Z12-environment) is promoted in presence of atoms exhibiting very similar size while a Z14-local ordering is an environment more advantageous for larger solute atoms which is likely the case here with the presence of Zr ([60]–[62]). The second idea is that it is also possible to nucleate Al-grains related by a twin relationship from a Z14-local ordering but on a limited number in comparison with a perfect icosahedral Z12-local ordering. Z14-local ordering is thus much less frequent in the liquid than Z12-icosahedral local ordering. To summarize, considering now that twin dendrites could nucleate from a Z14-local ordering it strongly decreases the possibility for such dendrites to develop because (i) there are much fewer Z14 environments in the liquid, and (ii) there are also fewer chances in a Z14-motif to nucleate the two orientations necessary to grow a twin dendrite. To further support our interpretation, the same alloy without Zirconium has been printed. An EBSD map of the alloy without Zr is shown in **Figure 12**. No twin dendrites were observed in the alloy version without Zr, a solute known to promote local ordering with coordination numbers larger than 12 in liquid Al, as is indicated by ab initio molecular dynamics calculations [58], [61].

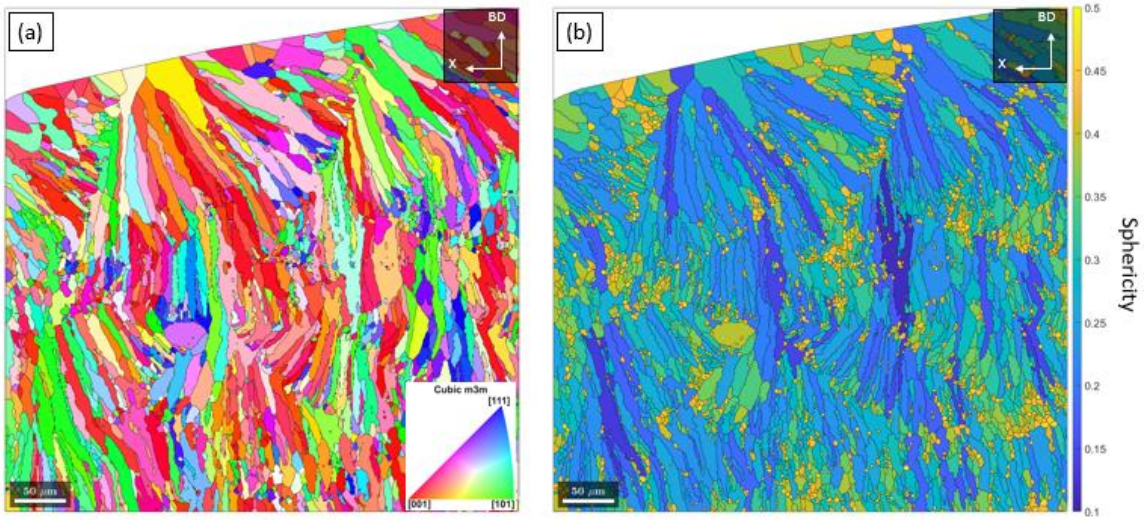

Figure 12 : Zr-free alloy microstructure: (a) IPF-EBSD map of aluminum parallel to the Building Direction (BD) (500 nm step size). (b) The grain sphericity map is obtained from (a). When sphericity is higher than 0.3 aluminum grains are considered equiaxed whereas for sphericity < 0.4 there are considered columnar. In the Zr-free alloy, fine size equiaxed grains are located along the melt pool boundaries. No twin dendrites have been observed in the Zr-free alloy.

In addition to the problem of twin dendrites nucleation, we also wish to comment on the growth competition between classical columnar grains and feathery grains in the NCZ, see **Figure 2**. Feathery grains exhibit a peculiar morphology and are associated with twin dendrites having their primary trunks growing along an uncommon <211>-direction (**Figure 8**). In columnar grains, dendrites have their primary trunks growing along the typical growth directions of FCC-metals, i.e. <100>-directions. To explain the variety of growth directions, our hypothesis is that some crystal

orientation growth directions promote the kinetics attachment of tetrahedral local packing at the solid/liquid interface as suggested by Kurtuldu *et al.* in [36]. As a result, all growth directions become nearly energetically equivalent resulting in non-classical growth directions such as <110> [63] or <320> in Al-Zn-Cr [64], or <211> in Al-Cu-Mg [65].
Twin dendrites also show well-developed secondary arms growing along <110>-directions though, in classical columnar grains, we noticed the absence of secondary arms. We do not believe that the presence of secondary arms in twin dendrites (feathery grains) could be explained by local variations of the solidification conditions because feathery grains were sometimes observed in the vicinity of columnar grains, see **Figure 2**. In other words, solidification conditions are not expected to differ significantly in two adjacent grains having a different morphology. As shown in the region highlighted in red in **Figure 6**, intermetallics were not only distributed in the interdendritic spaces but were also found decorating the twin plane separating the primary trunk. This observation is consistent with the morphology of the dendrite tip initially proposed by S. Henry *et al.* [65] and later confirmed by M. Salgado *et al.*[66] where solute pile-up creates a narrow channel of liquid in the center of a doublon dendrite. Solute enrichment in this narrow channel explains the formation of intermetallics along the twin plane and also accounts for the growth advantage of twin dendrites, the latter growing at a lower undercooling in comparison with classical dendrites which reject all the partitioned solutes ahead of the tip. Twin dendrites growth is also reported to be promoted by convective flows, see S. Henry [67]. Here, we would like to emphasize that convective flows in the molten bead during L-PBF are often reported in the literature, for example, due to the Marangoni effect. Thus, L-PBF processing conditions can be seen as a situation favorable for the growth of twin dendrites.

4.3. ISRO as a new alloy design strategy for AM materials

4.3.1. ISRO as a strategy to refine grain size: processability and grain boundary strengthening

High-performance alloys such as structural Al-alloys from the 2XXX, 6XXX, or 7XXX series ([12], [14]), or difficult-to-weld Ni-based superalloys ([68]–[70]) are strongly challenging to be processed by additive manufacturing due to the development of hot cracks. The most efficient way to increase hot cracking resistance consists in refining the grain size. Three different nucleation mechanisms have been identified, and two of them are closely related to ISRO. Manipulating ISRO-related nucleation mechanisms could be considered as a strategy to improve the AM processability of high-performance engineering alloys while taking advantage of a Hall-Petch strengthening effect (grain size < 1 μm).

For promoting heterogeneous nucleation on complex phases, solutes known to generate primary complex phases have to be sought. To do so, thermodynamic calculations could be useful to identify systems where complex primary phases or related quasicrystalline phases are expected to form.
In our alloy, we think that ISRO into the liquid is promoted by the interactions between the different alloying elements, in particular Al and Mn. The latter has an electronic structure with partially filled d-orbitals, a situation known to favor topological short-range order in the liquid by creating icosahedral clustering with Aluminum (see e.g. [71]). Besides, in the alloy without Zirconium, in addition to the absence of twin dendrites (**Figure 12**(a-b)), very few twin boundaries were found in the FEZ in comparison with the alloy with Zr. This suggests that Zr contributes to enhancing local liquid ordering. To promote ISRO-mediated nucleation, one could rely on *ab initio* calculations to predict atomic interactions and resulting atom clustering as done in [61], [62], [71]. However, to date, such *ab initio* computations are established for binary or ternary Al-based alloys, yet such calculations are highly challenging to perform for multi-constituted systems.

4.3.2. ISRO as a strategy to randomize texture

Microstructures inherited from AM processes often show strong morphological and crystallographic texture with columnar grains that can lead to anisotropic mechanical properties [72]. Thus, pathways to reduce this anisotropy should be considered interesting to make materials processed by AM more attractive. We discuss hereafter how ISRO enables the production of weaker morphological and crystallographic textures. We already discussed in the previous section how ISRO-related mechanisms can be exploited to produce equiaxed grains. Those grains necessarily contribute to breaking down the epitaxial growth of coarse columnar grains from the underlying layers and help to produce weaker crystallographic texture. However, in some modified high-strength alloys, such as the Zr-modified 6061 investigated in [20], a <100> texture can still develop in the columnar zone [73]. In this work, the Al-Mn-Ni-Cu-Zr alloy does not show a <100> texture in the NCZ. We establish some links between this weak texture and the presence of ISRO in the liquid. We suggest that a contribution to the weak texture in the NCZ may be the presence of twin dendrites (two orientations for a given dendrite) combined with the variety of growth directions as illustrated in **Figure 8**.

Thus, to integrate those results in an alloy design strategy, one way is to create conditions favorable for the nucleation and growth of twin dendrites. Increasing the proportion of Z14-local ordering into the liquid seems to promote both nucleation and growth of twin dendrites. Metal transition elements with larger atomic sizes could be considered. Indeed, such metal transition atoms are too large to be included in icosahedra but might be trapped in less closely packed local environments (Z14, Z15, or Z16). *Ab initio* calculations to investigate local ordering in undercooled liquids would also be helpful to identify solutes promoting Z14-local ordering. Finally, as convection was proven to promote the growth of twin dendrites, one could imagine taking advantage of the convective flows in the molten bead during L-PBF.

4.3.3. Other consequences of ISRO

Although our alloy is much more complicated than model binary systems investigated in the literature using *ab initio* MD calculations because it contains 4 different solutes (Mn, Ni, Cu, and Zr), we still believe that the results inferred from such computations are useful to qualitatively discuss the other possible consequences of promoting ISRO during additive manufacturing. We would firstly remind the link between the chemical and structural order, and the dynamic properties of liquid Al-alloys, especially in the undercooled regime. The work of Pasturel and Jakse [71] suggested that the liquid phase could be seen as a heterogeneous medium consisting of (i) regions with ISRO that can possibly extend to IMRO, and (ii) regions with a crystal-like ordering. Interestingly, depending on the respective proportion of local ordering (icosahedral vs. crystal-like ordering), important consequences on the dynamic properties, namely, viscosity and diffusivity are expected. Considering that we have a large proportion of ISRO in the liquid in our alloy processed by L-PBF, we propose to discuss what could be the consequences of an increase in viscosity and slower diffusivity.

In section 3.1., defects have been classified into two populations: the spherical ones that are typical of gas pores, and the tortuous ones as shown by **Figure 1**(c) that can be considered as micro shrinkages forming in the intergranular regions in the FEZ. Based on [59], [62], [71], [74], we expect an increase of viscosity in the presence of a large proportion of ISRO giving to the liquid a non-Arrhenius behavior. Here, we suggest that this increase in viscosity combined with the presence of a high fraction of intermetallics (**Figure 1**(c)) and small interdendritic channels makes liquid feeding more difficult. Therefore, ISRO into the liquid indirectly promotes the formation of tortuous pores identified as micro shrinkage using nano-CT scans. Also, the presence of narrow bands consisting of fine equiaxed grains at the center of the melt pools can be seen as an indirect signature of the high viscosity of the melt. Here, we believe that convective flow leaves a microstructural signature due to an increased melt viscosity caused by ISRO in the liquid. Overall, this increase of viscosity induced by ISRO in the melt can be seen as a drawback as it makes it more difficult to liquid feeding and thus

leads to the formation of micro shrinkages. However, one has to keep in mind that ISRO also contributes to the refinement of the microstructure, so those micro shrinkages are very small, typically of the order of 1 micron, and should not be as detrimental to the mechanical properties, as the large shrinkage pores usually observed in cast products.

Local ordering in the liquid is also expected to decrease the diffusivity of solutes through a cage effect, see e.g. [59], [62], [71], [74]. This idea was supported by Kurtuldu *et al.* [74] who have studied the influence of Cr on the diffusion in Al-Zn liquids. They found a slower diffusivity of Zn in presence of Cr which was justified by the diffusion of icosahedral clusters instead of individual atoms into the liquid (cage effect). In the framework of additive manufacturing, decreasing the diffusivity of solutes is an interesting pathway to extend supersaturation at lower solid-liquid interface velocities. Extended supersaturations in as-built products can be of particular interest in alloying systems such as high-strength Al-alloys, Ni-based superalloys, and generally speaking for precipitation-strengthened alloys, where precipitation strengthening is sought for. Achieving supersaturated solid solutions in as-built conditions can also be seen as an interesting pathway to reduce post-fabrication heat treatments as there is no need for solutionizing and quenching. We plan to further investigate such a phenomenon by investigating the atomic scale local chemical heterogeneities in the solid solutions using atom probe tomography coupled with HR-TEM.

As a final remark, we would like to point out the fact that intermetallic complex phases containing icosahedral building blocks are usually locally closely packed phases in which diffusion is relatively slow in comparison with simpler crystalline phases ([75], [76]). Such phases are often considered coarsening-resistant ([74], [75]). Those phases are very fine in the as-built conditions because of the high cooling rates of L-PBF and can be kept fine after long thermal exposure. Thus, one could imagine promoting their formation for the sake of thermal stability.

5. Conclusion

Through an advanced characterization of the microstructure, we reveal a multiscale hierarchical microstructure composed of alternating zones with fine equiaxed grains (FEZ) or with complex entanglements of columnar grains or coarser equiaxed grains (NCZ). Microstructural features evidenced in each zone question nucleation mechanisms involved in the FEZ and growth mechanisms in the NCZ since a high content of twin boundaries is observed in our alloy. Through automated crystal orientation mapping in TEM and nano-XCT, we have obtained the three following main results:

- Three nucleation different mechanisms have been identified: epitaxial nucleation on the $L1_2$-Al_3Zr primary phase, epitaxial nucleation on the complex $Al_{60}Mn_{11}Ni_4$ primary phase, and ISRO-mediated nucleation. The last two account for the high content of Σ3 twin boundaries within the FEZ.
- Twin dendrites with primary trunks growing along a <211> direction and secondary arms growing along a <110>-direction have been found.
- The origin of twin dendrites has been clarified thanks to a 3D nanoscale characterization using nano-XCT showing that such dendrites nucleate from the FEZ. We propose that such dendrites nucleate from a Z14 local ordering in the liquid.

We have discussed the multiple positive consequences of ISRO in the liquid on the as-built microstructure. This can be summarized as follows:

- ISRO is an efficient strategy to refine the grain size. Fine grains are desirable (i) to improve the processability via an increase of the hot cracking resistance, (ii) to increase the mechanical properties at room temperature via Hall-Petch strengthening.
- ISRO can be used to break down the strong morphological and crystallographic texture usually observed in additively manufactured parts by promoting nucleation of equiaxed grains without losing supersaturation and randomizing the texture of columnar grains thanks to twinned dendrites. This can be seen as an interesting pathway to achieve more isotropic properties.

We conclude that alloy design strategies aiming at promoting ISRO in the liquid during additive manufacturing of engineering alloys should be considered a serious and promising route toward optimized properties.

Data availability

The raw/processed data required to reproduce these findings cannot be shared at this time as the data also forms part of an ongoing study.

Acknowledgements

The authors are grateful to the AEROPRINT project supported by the Région Rhône-Alpes Auvergne. This work has benefited from the characterization equipment of the Grenoble INP - CMTC platform supported by the Centre of Excellence of Multifunctional Architectured Materials "CEMAM" n°ANR-10-LABX-44-01 funded by the Investments for the Future program. The European Synchrotron Radiation Facility (ESRF) is gratefully acknowledged for offering beamtime at ID16B associated with proposal MA4632-MA5086. The authors would like to thank Alain Pasturel and Noel Jakse for fruitful discussions.

References

[1] Z. Zhu *et al.*, « Superior mechanical properties of a selective-laser-melted AlZnMgCuScZr alloy enabled by a tunable hierarchical microstructure and dual-nanoprecipitation », *Materials Today*, vol. 52, p. 90‑ 101, janv. 2022, doi: 10.1016/j.mattod.2021.11.019.

[2] A. Bandyopadhyay, K. D. Traxel, M. Lang, M. Juhasz, N. Eliaz, et S. Bose, « Alloy design via additive manufacturing: Advantages, challenges, applications and perspectives », *Materials Today*, vol. 52, p. 207‑ 224, janv. 2022, doi: 10.1016/j.mattod.2021.11.026.

[3] Q. Jia, P. Rometsch, S. Cao, K. Zhang, et X. Wu, « Towards a high strength aluminium alloy development methodology for selective laser melting », *Materials & Design*, vol. 174, p. 107775, juill. 2019, doi: 10.1016/j.matdes.2019.107775.

[4] R. A. Michi, A. Plotkowski, A. Shyam, R. R. Dehoff, et S. S. Babu, « Towards high-temperature applications of aluminium alloys enabled by additive manufacturing », *International Materials Reviews*, vol. 67, n° 3, p. 298‑ 345, avr. 2022, doi: 10.1080/09506608.2021.1951580.

[5] M. Wang, B. Song, Q. Wei, Y. Zhang, et Y. Shi, « Effects of annealing on the microstructure and mechanical properties of selective laser melted AlSi7Mg alloy », *Materials Science and Engineering: A*, vol. 739, p. 463‑ 472, janv. 2019, doi: 10.1016/j.msea.2018.10.047.

[6] J. G. Santos Macías, T. Douillard, L. Zhao, E. Maire, G. Pyka, et A. Simar, « Influence on microstructure, strength and ductility of build platform temperature during laser powder bed fusion of AlSi10Mg », *Acta Materialia*, vol. 201, p. 231‑ 243, déc. 2020, doi: 10.1016/j.actamat.2020.10.001.

[7] K. G. Prashanth, S. Scudino, et J. Eckert, « Defining the tensile properties of Al-12Si parts produced by selective laser melting », *Acta Materialia*, vol. 126, p. 25‑ 35, mars 2017, doi: 10.1016/j.actamat.2016.12.044.
[8] Z. Hu, X. Nie, Y. Qi, H. Zhang, et H. Zhu, « Cracking criterion for high strength Al–Cu alloys fabricated by selective laser melting », *Additive Manufacturing*, vol. 37, p. 101709, janv. 2021, doi: 10.1016/j.addma.2020.101709.
[9] J. Deng, C. Chen, W. Zhang, Y. Li, R. Li, et K. Zhou, « Densification, Microstructure, and Mechanical Properties of Additively Manufactured 2124 Al–Cu Alloy by Selective Laser Melting », *Materials*, vol. 13, n° 19, Art. n° 19, janv. 2020, doi: 10.3390/ma13194423.
[10] F. Xiao *et al.*, « Niobium nanoparticle-enabled grain refinement of a crack-free high strength Al-Zn-Mg-Cu alloy manufactured by selective laser melting », *Journal of Alloys and Compounds*, vol. 900, p. 163427, avr. 2022, doi: 10.1016/j.jallcom.2021.163427.
[11] R. Casati, M. Coduri, M. Riccio, A. Rizzi, et M. Vedani, « Development of a high strength Al–Zn–Si–Mg–Cu alloy for selective laser melting », *Journal of Alloys and Compounds*, vol. 801, p. 243‑ 253, sept. 2019, doi: 10.1016/j.jallcom.2019.06.123.
[12] A. Sonawane, G. Roux, J.-J. Blandin, A. Despres, et G. Martin, « Cracking mechanism and its sensitivity to processing conditions during laser powder bed fusion of a structural Aluminum alloy. », *Materialia*, p. 100976, déc. 2020, doi: 10.1016/j.mtla.2020.100976.
[13] S. Z. Uddin, L. E. Murr, C. A. Terrazas, P. Morton, D. A. Roberson, et R. B. Wicker, « Processing and characterization of crack-free aluminum 6061 using high-temperature heating in laser powder bed fusion additive manufacturing », *Additive Manufacturing*, vol. 22, p. 405‑ 415, août 2018, doi: 10.1016/j.addma.2018.05.047.
[14] T. M. Pollock, J. Martin, B. D. Yahata, J. M. Hundley, J. A. Mayer, et T. A. Schaedler, « 3D printing of high-strength aluminium alloys », *Nature*, vol. 549, p. 365‑ 369, 2017.
[15] S. Y. Zhou, Y. Su, H. Wang, J. Enz, T. Ebel, et M. Yan, « Selective laser melting additive manufacturing of 7xxx series Al-Zn-Mg-Cu alloy: Cracking elimination by co-incorporation of Si and TiB2 », *Additive Manufacturing*, vol. 36, p. 101458, déc. 2020, doi: 10.1016/j.addma.2020.101458.
[16] X. Wen *et al.*, « Laser solid forming additive manufacturing TiB2 reinforced 2024Al composite: Microstructure and mechanical properties », *Materials Science and Engineering: A*, vol. 745, p. 319‑ 325, févr. 2019, doi: 10.1016/j.msea.2018.12.072.
[17] Q. Tan, Y. Yin, Z. Fan, J. Zhang, Y. Liu, et M.-X. Zhang, « Uncovering the roles of LaB6-nanoparticle inoculant in the AlSi10Mg alloy fabricated via selective laser melting », *Materials Science and Engineering: A*, vol. 800, p. 140365, janv. 2021, doi: 10.1016/j.msea.2020.140365.
[18] Q. Tan *et al.*, « A novel method to 3D-print fine-grained AlSi10Mg alloy with isotropic properties via inoculation with LaB6 nanoparticles », *Additive Manufacturing*, vol. 32, p. 101034, mars 2020, doi: 10.1016/j.addma.2019.101034.
[19] H. Zhang, H. Zhu, X. Nie, J. Yin, Z. Hu, et X. Zeng, « Effect of Zirconium addition on crack, microstructure and mechanical behavior of selective laser melted Al-Cu-Mg alloy », *Scripta Materialia*, vol. 134, p. 6‑ 10, juin 2017, doi: 10.1016/j.scriptamat.2017.02.036.
[20] A. Mehta *et al.*, « Additive manufacturing and mechanical properties of the dense and crack free Zr-modified aluminum alloy 6061 fabricated by the laser-powder bed fusion », *Additive Manufacturing*, vol. 41, p. 101966, mai 2021, doi: 10.1016/j.addma.2021.101966.
[21] Q. Jia, P. Rometsch, S. Cao, K. Zhang, A. Huang, et X. Wu, « Characterisation of AlScZr and AlErZr alloys processed by rapid laser melting », *Scripta Materialia*, vol. 151, p. 42‑ 46, juill. 2018, doi: 10.1016/j.scriptamat.2018.03.035.
[22] S. Griffiths, M. D. Rossell, J. Croteau, N. Q. Vo, D. C. Dunand, et C. Leinenbach, « Effect of laser rescanning on the grain microstructure of a selective laser melted Al-Mg-Zr alloy », *Materials Characterization*, vol. 143, p. 34‑ 42, sept. 2018, doi: 10.1016/j.matchar.2018.03.033.
[23] X. Nie *et al.*, « Effect of Zr content on formability, microstructure and mechanical properties of selective laser melted Zr modified Al-4.24Cu-1.97Mg-0.56Mn alloys », *Journal of Alloys and Compounds*, oct. 2018, doi: 10.1016/J.JALLCOM.2018.06.032.
[24] A. B. Spierings *et al.*, « Microstructural features of Sc- and Zr-modified Al-Mg alloys processed by selective laser melting », *Materials & Design*, vol. 115, p. 52‑ 63, févr. 2017, doi: 10.1016/j.matdes.2016.11.040.

[25] K. V. Yang, Y. Shi, F. Palm, X. Wu, et P. Rometsch, « Columnar to equiaxed transition in Al-Mg(-Sc)-Zr alloys produced by selective laser melting », *Scripta Materialia*, vol. 145, p. 113‑117, mars 2018, doi: 10.1016/j.scriptamat.2017.10.021.
[26] Q. Jia *et al.*, « Selective laser melting of a high strength AlMnSc alloy: Alloy design and strengthening mechanisms », *Acta Materialia*, vol. 171, p. 108‑118, juin 2019, doi: 10.1016/j.actamat.2019.04.014.
[27] F. Leijon, S. Wachter, Z. Fu, C. Körner, S. Skjervold, et J. Moverare, « A novel rapid alloy development method towards powder bed additive manufacturing, demonstrated for binary Al-Ti, -Zr and -Nb alloys », *Materials & Design*, vol. 211, p. 110129, déc. 2021, doi: 10.1016/j.matdes.2021.110129.
[28] M. Roscher, S. Balachandran, D. Mayweg, et E. Jägle, « Development of Al-Ti-based alloys for laser powder bed fusion », *Additive Manufacturing*, vol. 47, p. 102315, nov. 2021, doi: 10.1016/j.addma.2021.102315.
[29] J. Zhang *et al.*, « A novel crack-free Ti-modified Al-Cu-Mg alloy designed for selective laser melting », *Additive Manufacturing*, vol. 38, p. 101829, févr. 2021, doi: 10.1016/j.addma.2020.101829.
[30] B. L. Bramfitt, « The effect of carbide and nitride additions on the heterogeneous nucleation behavior of liquid iron », *Metallurgical Transactions*, vol. 1, p. 1987‑1995, 1970, doi: https://doi.org/10.1007/BF02642799.
[31] D. Turnbull et B. Vernnegut, « Nucleation Catalysis », vol. 44, p. 1292‑1298, 1952, doi: https://doi.org/10.1021/ie50510a031.
[32] F. C. Frank et J. S. Kasper, « Complex alloy structures regarded as sphere packings. I. Definitions and basic principles », *Acta Cryst*, vol. 11, n° 3, p. 184‑190, mars 1958, doi: 10.1107/S0365110X58000487.
[33] D. Shechtman, I. Blech, D. Gratias, et J. W. Cahn, « Metallic Phase with Long-Range Orientational Order and No Translational Symmetry », *Phys. Rev. Lett.*, vol. 53, n° 20, p. 1951‑1953, nov. 1984, doi: 10.1103/PhysRevLett.53.1951.
[34] A. Hirata *et al.*, « Geometric Frustration of Icosahedron in Metallic Glasses », *Science*, vol. 341, n° 6144, p. 376‑379, juill. 2013, doi: 10.1126/science.1232450.
[35] H. W. Sheng, W. K. Luo, F. M. Alamgir, J. M. Bai, et E. Ma, « Atomic packing and short-to-medium-range order in metallic glasses », *Nature*, vol. 439, n° 7075, Art. n° 7075, janv. 2006, doi: 10.1038/nature04421.
[36] M. Rappaz, Ph. Jarry, G. Kurtuldu, et J. Zollinger, « Solidification of Metallic Alloys: Does the Structure of the Liquid Matter? », *Metall Mater Trans A*, vol. 51, n° 6, p. 2651‑2664, juin 2020, doi: 10.1007/s11661-020-05770-9.
[37] G. Kurtuldu, P. Jarry, et M. Rappaz, « Influence of Cr on the nucleation of primary Al and formation of twinned dendrites in Al–Zn–Cr alloys: Can icosahedral solid clusters play a role? », *Acta Materialia*, vol. 61, n° 19, p. 7098‑7108, nov. 2013, doi: 10.1016/j.actamat.2013.07.056.
[38] G. Kurtuldu, A. Sicco, et M. Rappaz, « Icosahedral quasicrystal-enhanced nucleation of the fcc phase in liquid gold alloys », *Acta Materialia*, vol. 70, p. 240‑248, mai 2014, doi: 10.1016/j.actamat.2014.02.037.
[39] M. Buttard *et al.*, « Multi-scale microstuctural investigation of a new Al-Mn-Ni-Cu-Zr aluminium alloy processed by laser powder bed fusion », *Materialia*, vol. 18, p. 101160, août 2021, doi: 10.1016/j.mtla.2021.101160.
[40] M. L. Montero-Sistiaga, C. Galera-Rueda, K. Vanmeensel, M. Godino-Martínez, J. Llorca, et M. T. Pérez-Prado, « Icosahedral quasicrystal-enhanced nucleation in Al alloys fabricated by selective laser melting », *Additive Manufacturing*, vol. 44, p. 102053, août 2021, doi: 10.1016/j.addma.2021.102053.
[41] C. Galera-Rueda, X. Jin, J. LLorca, et M. T. Pérez-Prado, « Icosahedral quasicrystal enhanced nucleation in commercially pure Ni processed by selective laser melting », *Scripta Materialia*, vol. 211, p. 114512, avr. 2022, doi: 10.1016/j.scriptamat.2022.114512.
[42] J. Zollinger, I. Cazic, S. Mathieu, M. El Kandaoui, P. Plapper, et B. Appolaire, « New insights into the origin of fine equiaxed microstructures in additively manufactured Inconel 718 », *Scripta Materialia*, vol. 195, p. 113740, avr. 2021, doi: 10.1016/j.scriptamat.2021.113740.

[43] S. Fan *et al.*, « Using grain boundary irregularity to quantify dynamic recrystallization in ice », *Acta Materialia*, vol. 209, p. 116810, mai 2021, doi: 10.1016/j.actamat.2021.116810.
[44] E. F. Rauch et M. Véron, « Automated crystal orientation and phase mapping in TEM », *Materials Characterization*, vol. 98, p. 1‑9, déc. 2014, doi: 10.1016/j.matchar.2014.08.010.
[45] E. F. Rauch, J. Portillo, S. Nicolopoulos, D. Bultreys, S. Rouvimov, et P. Moeck, « Automated nanocrystal orientation and phase mapping in the transmission electron microscope on the basis of precession electron diffraction », *Zeitschrift für Kristallographie*, vol. 225, n° 2‑3, p. 103‑109, mars 2010, doi: 10.1524/zkri.2010.1205.
[46] E. F. Rauch, P. Harrison, X. Zhou, M. Herbig, W. Ludwig, et M. Véron, « New Features in Crystal Orientation and Phase Mapping for Transmission Electron Microscopy », *Symmetry*, vol. 13, n° 9, Art. n° 9, sept. 2021, doi: 10.3390/sym13091675.
[47] G. Martínez-Criado *et al.*, « ID16B: a hard X-ray nanoprobe beamline at the ESRF for nano-analysis », *J Synchrotron Rad*, vol. 23, n° 1, Art. n° 1, janv. 2016, doi: 10.1107/S1600577515019839.
[48] P. Cloetens *et al.*, « Holotomography: Quantitative phase tomography with micrometer resolution using hard synchrotron radiation x rays », *Appl. Phys. Lett.*, vol. 75, n° 19, p. 2912‑2914, nov. 1999, doi: 10.1063/1.125225.
[49] A. Mirone, E. Gouillart, E. Brun, P. Tafforeau, et J. Kieffer, « PyHST2: an hybrid distributed code for high speed tomographic reconstruction with iterative reconstruction and a priori knowledge capabilities », *Nuclear Instruments and Methods in Physics Research Section B: Beam Interactions with Materials and Atoms*, vol. 324, p. 41‑48, avr. 2014, doi: 10.1016/j.nimb.2013.09.030.
[50] T. J⁄ssang et J. P. Hirth, « The energies of stacking-fault teirahedra in f.c.c. metals », *The Philosophical Magazine: A Journal of Theoretical Experimental and Applied Physics*, vol. 13, n° 124, p. 657‑670, avr. 1966, doi: 10.1080/14786436608212687.
[51] I. L. Dillamore et R. E. Smallman, « The stacking-fault energy of F.C.C. metals », *The Philosophical Magazine: A Journal of Theoretical Experimental and Applied Physics*, vol. 12, n° 115, p. 191‑193, juill. 1965, doi: 10.1080/14786436508224959.
[52] T. C. Schulthess, P. E. A. Turchi, A. Gonis, et T.-G. Nieh, « Systematic study of stacking fault energies of random Al-based alloys », *Acta Materialia*, vol. 46, n° 6, p. 2215‑2221, mars 1998, doi: 10.1016/S1359-6454(97)00432-1.
[53] M. Muzyk, Z. Pakiela, et K. J. Kurzydlowski, « Ab initio calculations of the generalized stacking fault energy in aluminium alloys », *Scripta Materialia*, vol. 64, n° 9, p. 916‑918, mai 2011, doi: 10.1016/j.scriptamat.2011.01.034.
[54] G. Kurtuldu, P. Jarry, et M. Rappaz, « Influence of Cr on the nucleation of primary Al and formation of twinned dendrites in Al–Zn–Cr alloys: Can icosahedral solid clusters play a role? », *Acta Materialia*, vol. 61, n° 19, p. 7098‑7108, nov. 2013, doi: 10.1016/j.actamat.2013.07.056.
[55] R. S. Mishra et S. Thapliyal, « Design approaches for printability-performance synergy in Al alloys for laser-powder bed additive manufacturing », *Materials & Design*, vol. 204, p. 109640, juin 2021, doi: 10.1016/j.matdes.2021.109640.
[56] K. F. Kelton, « Quasicrystals: structure and stability », *International Materials Reviews*, vol. 38, n° 3, p. 105‑137, janv. 1993, doi: 10.1179/imr.1993.38.3.105.
[57] N. Senabulya et A. J. Shahani, « Growth interactions between icosahedral quasicrystals », *Phys. Rev. Materials*, vol. 3, n° 9, p. 093403, sept. 2019, doi: 10.1103/PhysRevMaterials.3.093403.
[58] M. J. Kramer et M. Li, « Changes in short- and medium-range order in metallic liquids during undercooling », *MRS Bulletin*, vol. 45, n° 11, p. 943‑950, nov. 2020, doi: 10.1557/mrs.2020.272.
[59] N. Jakse et A. Pasturel, « Correlation between dynamic slowing down and local icosahedral ordering in undercooled liquid Al80Ni20 alloy », *J. Chem. Phys.*, vol. 143, n° 8, p. 084508, août 2015, doi: 10.1063/1.4929481.
[60] N. Jakse, O. Le Bacq, et A. Pasturel, « Chemical and icosahedral short-range orders in liquid and undercooled Al80Mn20 and Al80Ni20 alloys: A first-principles-based approach », *J. Chem. Phys.*, vol. 123, n° 10, p. 104508, sept. 2005, doi: 10.1063/1.1979495.
[61] A. Pasturel et N. Jakse, « Structural and dynamic properties of liquid CuxZr1-x alloys by ab initio molecular dynamics », *Physical Review B: Condensed Matter and Materials Physics (1998-2015)*, vol. 78, p. 214204, 2008.

[62] N. Jakse, O. Lebacq, et A. Pasturel, « Ab Initio Molecular-Dynamics Simulations of Short-Range Order in Liquid Al80Mn20 Al80Ni20 alloys. », *Phys. Rev. Lett.*, vol. 93, n° 20, p. 207801, nov. 2004, doi: 10.1103/PhysRevLett.93.207801.
[63] T. Haxhimali, A. Karma, F. Gonzales, et M. Rappaz, « Orientation selection in dendritic evolution », *Nature Mater*, vol. 5, n° 8, Art. n° 8, août 2006, doi: 10.1038/nmat1693.
[64] A. Sémoroz, Y. Durandet, et M. Rappaz, « EBSD characterization of dendrite growth directions, texture and misorientations in hot-dipped Al–Zn–Si coatings », *Acta Materialia*, vol. 49, n° 3, p. 529‑541, févr. 2001, doi: 10.1016/S1359-6454(00)00322-0.
[65] S. Henry, T. Minghetti, et M. Rappaz, « Dendrite growth morphologies in aluminium alloys », *Acta Materialia*, vol. 46, n° 18, p. 6431‑6443, nov. 1998, doi: 10.1016/S1359-6454(98)00308-5.
[66] M. A. Salgado-Ordorica, P. Burdet, M. Cantoni, et M. Rappaz, « Study of the twinned dendrite tip shape II: Experimental assessment », *Acta Materialia*, vol. 59, n° 13, p. 5085‑5091, août 2011, doi: 10.1016/j.actamat.2011.04.034.
[67] S. Henry, G.-U. Gruen, et M. Rappaz, « Influence of convection on feathery grain formation in aluminum alloys », *Metall and Mat Trans A*, vol. 35, n° 8, p. 2495‑2501, août 2004, doi: 10.1007/s11661-006-0229-1.
[68] A. Després *et al.*, « On the role of boron, carbon and zirconium on hot cracking and creep resistance of an additively manufactured polycrystalline superalloy », *Materialia*, vol. 19, p. 101193, sept. 2021, doi: 10.1016/j.mtla.2021.101193.
[69] A. Hariharan *et al.*, « Misorientation-dependent solute enrichment at interfaces and its contribution to defect formation mechanisms during laser additive manufacturing of superalloys », *Phys. Rev. Materials*, vol. 3, n° 12, p. 123602, déc. 2019, doi: 10.1103/PhysRevMaterials.3.123602.
[70] E. Chauvet *et al.*, « Hot cracking mechanism affecting a non-weldable Ni-based superalloy produced by selective electron Beam Melting », *Acta Materialia*, vol. 142, p. 82‑94, janv. 2018, doi: 10.1016/j.actamat.2017.09.047.
[71] A. Pasturel et N. Jakse, « Influence of Cr on local order and dynamic properties of liquid and undercooled Al–Zn alloys », *J. Chem. Phys.*, vol. 146, n° 18, p. 184502, mai 2017, doi: 10.1063/1.4982887.
[72] Y. Kok *et al.*, « Anisotropy and heterogeneity of microstructure and mechanical properties in metal additive manufacturing: A critical review », *Materials & Design*, vol. 139, p. 565‑586, févr. 2018, doi: 10.1016/j.matdes.2017.11.021.
[73] M. Opprecht, J.-P. Garandet, G. Roux, C. Flament, et M. Soulier, « A solution to the hot cracking problem for aluminium alloys manufactured by laser beam melting », *Acta Materialia*, vol. 197, p. 40‑53, sept. 2020, doi: 10.1016/j.actamat.2020.07.015.
[74] G. Kurtuldu, P. Jarry, et M. Rappaz, « Influence of icosahedral short range order on diffusion in liquids: A study on Al-Zn-Cr alloys », *Acta Materialia*, vol. 115, p. 423‑433, août 2016, doi: 10.1016/j.actamat.2016.05.051.
[75] J.-O. Nilsson, A. Hultin Stigenberg, et P. Liu, « Isothermal formation of quasicrystalline precipitates and their effect on strength in a 12Cr-9Ni-4Mo maraging stainless steel », *Metall Mater Trans A*, vol. 25, n° 10, p. 2225‑2233, oct. 1994, doi: 10.1007/BF02652323.
[76] A. Singh, M. Watanabe, A. Kato, et A. P. Tsai, « Strengthening effects of icosahedral phase in magnesium alloys », *Philosophical Magazine*, vol. 86, n° 6‑8, p. 951‑956, févr. 2006, doi: 10.1080/14786430500253901.
[77] M. Pessah-Simonetti, P. Caron, et P. Donnadieu, « T. C. P. phase particles embedded in a superalloy matrix: Interpretation and prediction of the orientation relationships. [Topologically close packed] », *Scripta Metallurgica et Materialia; (United States)*, vol. 30:12, juin 1994, doi: 10.1016/0956-716X(94)90307-7.
[78] D. H. Bae, S. H. Kim, D. H. Kim, et W. T. Kim, « Deformation behavior of Mg–Zn–Y alloys reinforced by icosahedral quasicrystalline particles », *Acta Materialia*, vol. 50, n° 9, p. 2343‑2356, mai 2002, doi: 10.1016/S1359-6454(02)00067-8.

SUPPLEMENTARY

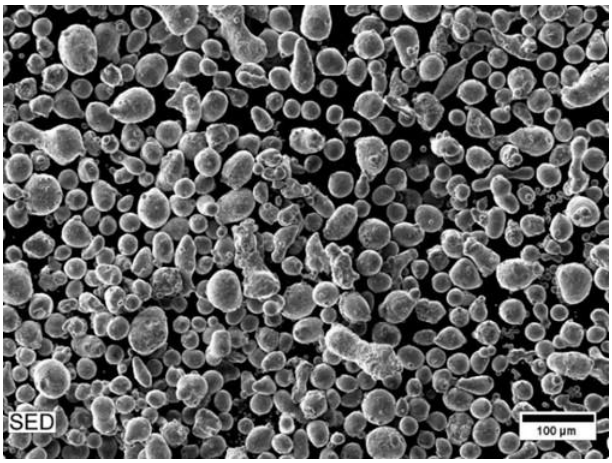

Figure S 1 : SEM micrograph illustrating the morphology and size of the as-received gas atomized powder.

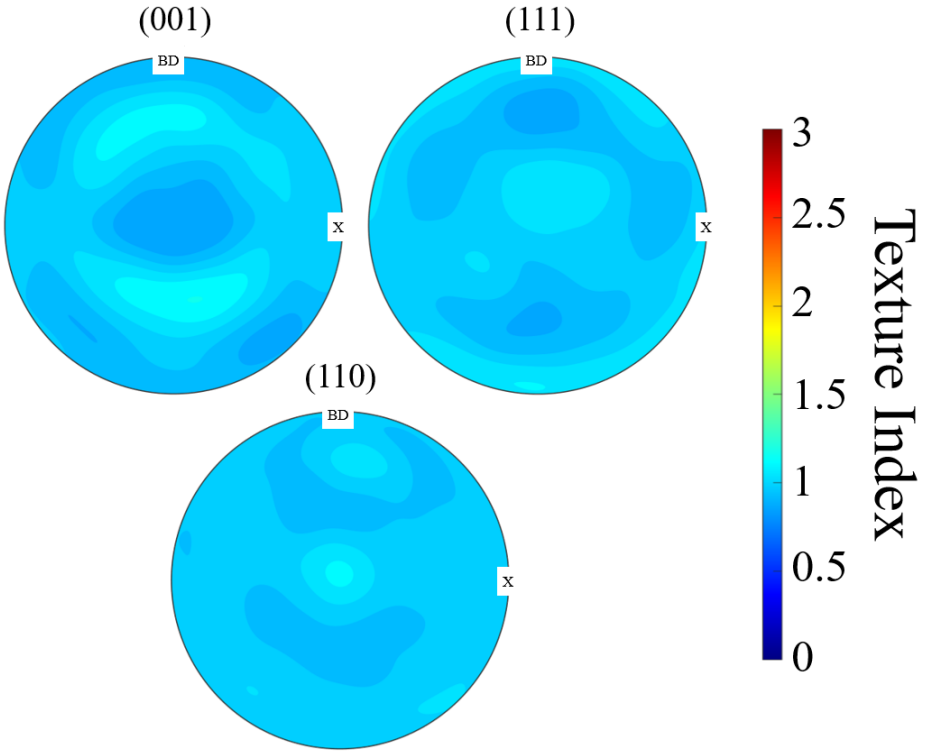

Figure S 2 : (001), (110) and (111) poles figures were plotted considering only columnar grains (ψ<0.35) in the Figure 2.

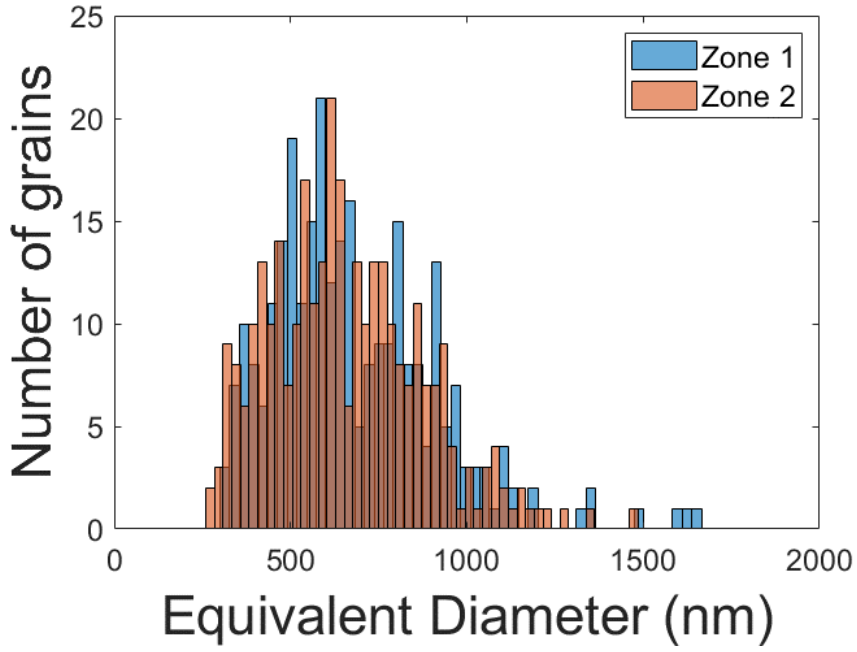

Figure S 3 : Distribution of the equivalent diameter of matrix grains within the fine equiaxed zone (FEZ). Two different regions of interest have been selected for statistical consistency. One of them is represented in Figure 6. The average grain size is equal to 610 nm while the standard deviation is relatively high (250 nm).

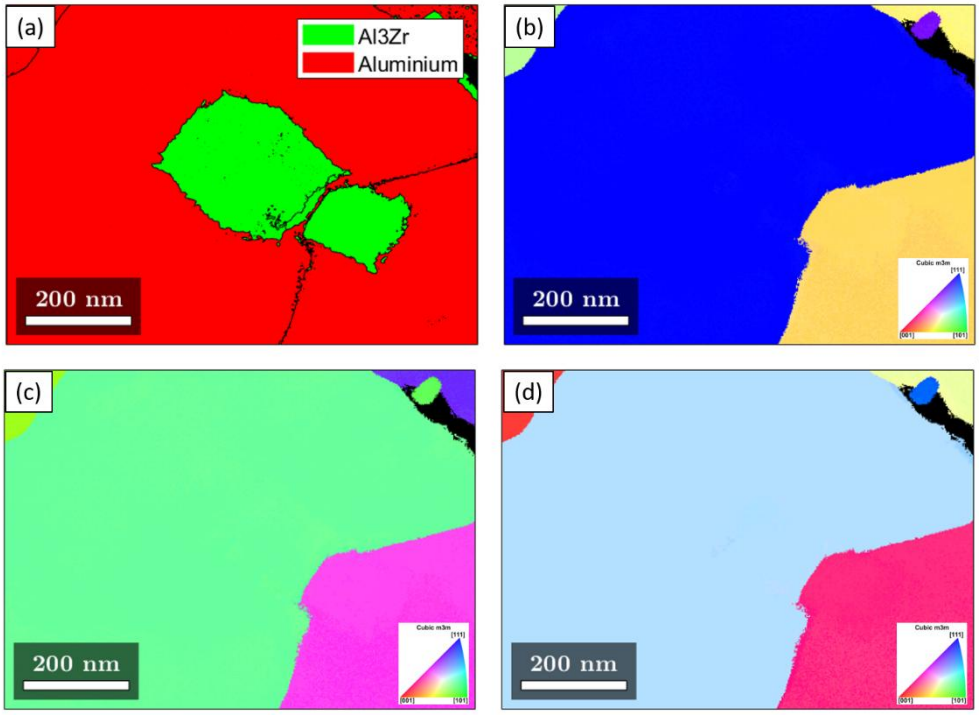

Figure S 4 : Local study of the phase distribution in the FEZ using ACOM. (a) Phase map of the region interest showing two Al_3Zr in two different aluminium grains. The orientation maps of the same region of interest normal to: (b) the X-direction (c) the Y-direction (d) the Z-direction reveal a cube-cube orientation relationship between a primary Al_3Zr prcipitate and the Aluminum matrix.

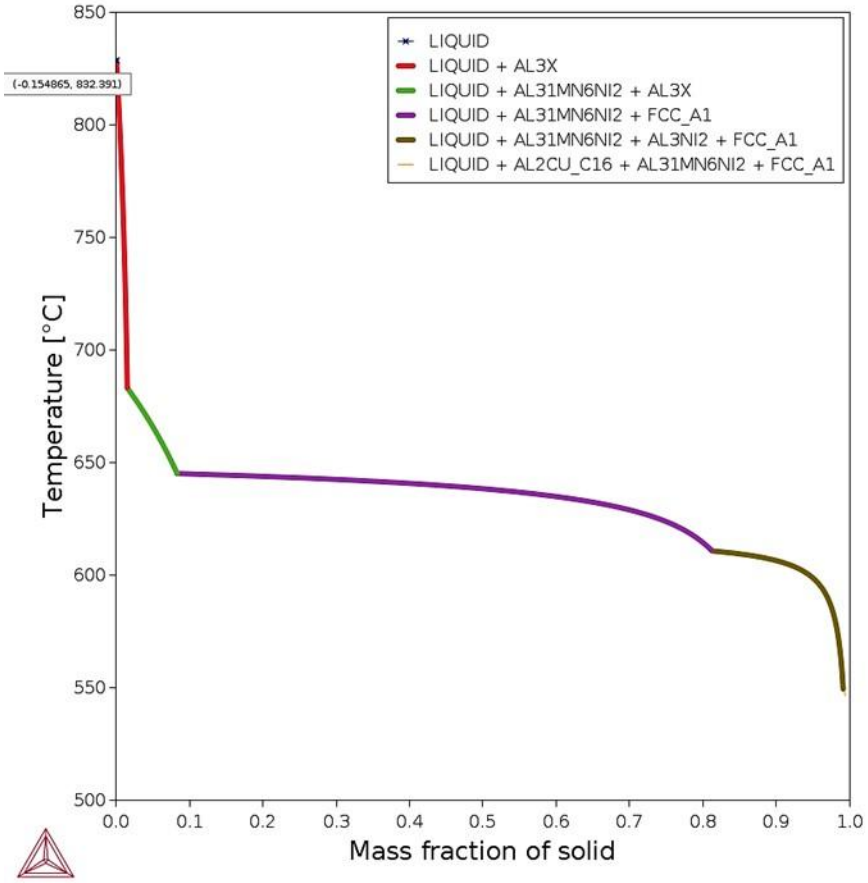

Figure S 5 : Thermodynamics Calculations obtained with Scheil Gulliver's model selecting only phases identified with XRD in the TCAL v6 database. The phases FCC_A1, Al_3X, and $Al_{31}Mn_6Ni_2$ corresponds respectively to the Al, Al_3Zr, and $Al_{60}Mn_{11}Ni_4$ phases.